



# Adiabatic Rearrangement of Hollow PV Towers

Eric A. Hendricks<sup>1</sup> and Wayne H. Schubert<sup>2</sup>

<sup>1</sup>Marine Meteorology Division, Naval Research Laboratory, Monterey, California, USA

<sup>2</sup>Department of Atmospheric Science, Colorado State University, Fort Collins, Colorado, USA

Manuscript submitted 15 March 2010; in final form 21 September 2010

Diabatic heating from deep moist convection in the hurricane eyewall produces a towering annular structure of elevated potential vorticity (PV). This structure has been referred to as a *hollow PV tower*. The sign reversal of the radial gradient of PV satisfies the Charney-Stern necessary condition for combined barotropic-baroclinic instability. For thin enough annular structures, small perturbations grow exponentially, extract energy from the mean flow, and lead to hollow tower breakdown, with significant vortex structural and intensity change. The three-dimensional adiabatic rearrangements of two prototypical hurricane-like hollow PV towers (one thick and one thin) are examined in an idealized framework. For both hollow towers, dynamic instability causes air parcels with high PV to be mixed into the eye preferentially at lower levels, where unstable PV wave growth rates are the largest. Little or no mixing is found to occur at upper levels. The mixing at lower and middle levels is most rapid for the breakdown of the thin hollow tower, consistent with previous barotropic results. For both hollow towers, this advective rearrangement of PV affects the tropical cyclone structure and intensity in a number of ways. First, the minimum central pressure and maximum azimuthal mean velocity simultaneously decrease, consistent with previous barotropic results. Secondly, isosurfaces of absolute angular momentum preferentially shift inward at low levels, implying an adiabatic mechanism by which hurricane eye-wall tilt can form. Thirdly, a PV bridge, similar to that previously found in full-physics hurricane simulations, develops as a result of mixing at the isentropic levels where unstable PV waves grow most rapidly. Finally, the balanced mass field resulting from the PV rearrangement is warmer in the eye between 900 and 700 hPa. The location of this warming is consistent with observed warm anomalies in the eye, indicating that in certain instances the hurricane eye inversion is enhanced through PV mixing on isentropic surfaces and is thus partially dynamically controlled.

DOI:10.3894/JAMES.2010.2.8

## 1. Introduction

One of the important challenges associated with tropical cyclone forecasting is rapid variability in structure and intensity. This is especially important when an intense hurricane is approaching a densely populated land mass. One dynamical mechanism known to produce such variability is potential vorticity (PV) mixing between the eyewall and the eye. PV in the eyewall is continually produced by deep cumulonimbus convection, resulting in a hollow tower structure that extends from the lower to middle troposphere (Schubert and Alworth 1987, Möller and Smith 1994). The sign reversal of the radial gradient of PV satisfies the Charney-Stern necessary condition for combined barotropic-baroclinic instability (Eliassen 1983, Montgomery and Shapiro 1995). If the ring of enhanced PV is narrow enough, the hollow tower may break down, causing air parcels with high PV to be mixed into the eye. Full-physics numerical simulations of hurricanes typically show high PV at lower levels of the eye, which can take

the form of a bridge (e.g., see Fig. 1, which is reproduced from Yau et al. 2004). Presumably, the high PV in the eye must have been mixed there from the eyewall, since there is no mechanism to generate such large PV in the eye once it has formed.

The calculation of hurricane inner-core PV from observations has been difficult due to sparseness of the data. The symmetric PV field in Hurricane Gloria (1985) was constructed by Shapiro and Franklin (1995) using wind analyses, dropwindsondes, and airborne Doppler radar data. While their data was not able to capture intricate details in the inner-core region, they were able to show large PV existed in the core, with a monotonic decrease moving radially outward to 500 km. More recently, Bell and Montgomery (2008) have calculated PV from *in situ* flight level and dropwindsonde observations of Hurricane Isabel (2003) in the inner-core region to approximately 4 km in height. Their results showed a hollow radial profile of PV with two maxima, at heights of approximately 1 and 3 km. The lower PV maximum was shown to be primarily

### To whom correspondence should be addressed.

Eric A. Hendricks, Marine Meteorology Division,  
Naval Research Laboratory, Monterey, CA 93940, USA  
eric.hendricks@nrlmry.navy.mil



This work is licensed under a Creative Commons Attribution 3.0 License.

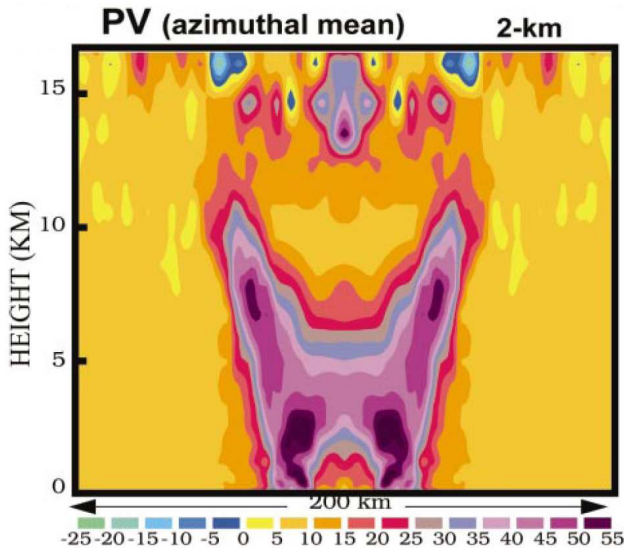


**Figure 1.** Azimuthal mean potential vorticity (in PV units) from a full-physics numerical simulation of Hurricane Andrew. Reproduced from Yau et al. (2004).

due to the large vorticity in the inner eyewall, while the PV maximum at 3 km was thought to have been enhanced by the large static stability associated with the thermal inversion layer in the eye. Moreover, the PV maximum at 3 km extended farther into the eye, creating a bridge-like structure similar to that found by Yau et al. (2004).

The barotropic or combined barotropic-baroclinic instability of hurricane-like vorticity rings and subsequent vorticity mixing has been the subject of a number of recent theoretical, numerical, observational and experimental studies (Guinn 1992, Schubert et al. 1999, Kossin and Schubert 2001, Kossin and Eastin 2001, Montgomery et al. 2002, Terwey and Montgomery 2002, Kossin et al. 2002, Nolan and Montgomery 2002, Nolan and Grasso 2003, Kossin and Schubert 2004, Rozoff et al. 2009, Hendricks et al. 2009). While much of this prior work has focused on examining vortex stability and asymmetric mixing in a barotropic framework, Nolan and Montgomery (2002), Nolan and Grasso (2003), Schechter and Montgomery (2004), and Hodyss and Nolan (2008) have examined the stability of three-dimensional tropical storm and hurricane-like vortices to unbalanced perturbations. An important conclusion of their work is that unstable modes on PV rings are often close analogs to their barotropic counterparts, although a more complicated Rossby-inertia-buoyancy type of instability can also occur on monotonic radial profiles of PV. Linear and nonlinear model simulations were also performed to examine both the effects of symmetric and asymmetric perturbations on vortex structure and intensity.

In the present work, we examine vortex structural and intensity change that can arise from dynamic instability of three-dimensional hurricane-like hollow PV towers in an unforced adiabatic framework. While diabatic heating in the eyewall generates and maintains the hollow tower, our goal is to understand the three-dimensional, adiabatic, PV mixing

process that ensues when the hollow towers break down. This work complements previous barotropic studies by examining PV mixing in a continuously stratified fluid. The PV mixing process is studied here in a dynamically clean framework by using an isentropic coordinate primitive equation model with minimal non-conservative effects. In this manner, the hurricane inner-core dynamics are examined in a canonical form by making PV maps on isentropic surfaces (Hoskins et al. 1985). In Section 2, we present the primitive equation model used in this study. The nonlinear evolution of the two prototypical hurricane-like hollow PV towers are presented and discussed in Section 3. In Section 4, azimuthal mean diagnostics of the simulations are presented to understand the relative roles of mean and eddy processes in the vortex structure and intensity change. Finally, the conclusions are given in Section 5.

## 2. Primitive equation model

### 2.1. Governing equations

We consider adiabatic, quasi-hydrostatic motions of a compressible atmosphere on an  $f$ -plane. Using the potential temperature  $\theta$  as the vertical coordinate, the equations for the eastward velocity component  $u$  and the northward velocity component  $v$  are

$$\frac{\partial u}{\partial t} - (f + \zeta)v + \frac{\partial}{\partial x} \left[ M + \frac{1}{2} (u^2 + v^2) \right] = 0, \quad (2.1)$$

$$\frac{\partial v}{\partial t} + (f + \zeta)u + \frac{\partial}{\partial y} \left[ M + \frac{1}{2} (u^2 + v^2) \right] = 0, \quad (2.2)$$

where  $\zeta = \partial v / \partial x - \partial u / \partial y$  is the isentropic relative vorticity,  $M = \theta \Pi + \Phi$  is the Montgomery potential,  $\Pi(p) = c_p (p/p_0)^\kappa$  is the Exner function,  $\Phi$  is the geopotential, and the Coriolis parameter is chosen to be  $f = 5 \times 10^{-5} \text{ s}^{-1}$ .

The numerical model used here is based on the vorticity/divergence form of the primitive equations. The equations for the isentropic relative vorticity and the isentropic divergence  $\delta = \partial u / \partial x + \partial v / \partial y$  are easily derived from (2.1) and (2.2), and can be written in the form

$$\frac{\partial \zeta}{\partial t} + \frac{\partial [(f + \zeta)u]}{\partial x} + \frac{\partial [(f + \zeta)v]}{\partial y} = 0, \quad (2.3)$$

$$\frac{\partial \delta}{\partial t} - \frac{\partial [(f + \zeta)v]}{\partial x} + \frac{\partial [(f + \zeta)u]}{\partial y} + \nabla^2 \left[ M + \frac{1}{2} (u^2 + v^2) \right] = 0, \quad (2.4)$$

where  $u, v, \zeta, \delta$  are expressed in terms of the velocity potential  $\chi$  and the streamfunction  $\psi$  as

$$u = \frac{\partial \chi}{\partial x} - \frac{\partial \psi}{\partial y}, \quad v = \frac{\partial \chi}{\partial y} + \frac{\partial \psi}{\partial x}, \quad (2.5)$$

$$\zeta = \nabla^2 \psi, \quad \delta = \nabla^2 \chi. \quad (2.6)$$

The hydrostatic and continuity equations are

$$\frac{\partial M}{\partial \theta} = \Pi, \quad (2.7)$$

$$\frac{\partial \sigma}{\partial t} + \frac{\partial(\sigma u)}{\partial x} + \frac{\partial(\sigma v)}{\partial y} = 0, \quad (2.8)$$

where  $\sigma = -g^{-1}(\partial p/\partial \theta)$  is the pseudodensity. Equations (2.3)–(2.8), along with the definitions of  $\sigma$  and  $\Pi$ , constitute a closed system in the three prognostic variables  $\zeta$ ,  $\delta$ ,  $\sigma$  and the seven diagnostic variables  $\chi$ ,  $\psi$ ,  $u$ ,  $v$ ,  $M$ ,  $\Pi$ ,  $p$ . Note that all variables are functions of  $x$ ,  $y$ ,  $\theta$ ,  $t$ , and all horizontal derivatives and time derivatives are taken on isentropic surfaces. Also note that a considerable simplification of the above equations has occurred because of the assumption  $\dot{\theta} = 0$ .

The potential vorticity principle, obtained by eliminating the isentropic divergence between (2.3) and (2.8), is

$$\frac{DP}{Dt} = 0, \quad (2.9)$$

where  $P = (f + \zeta)/\sigma$  is the potential vorticity, and where  $D/Dt = (\partial/\partial t) + u(\partial/\partial x) + v(\partial/\partial y)$  is the material derivative. This material conservation relation indicates that the system (2.3)–(2.8) describes the PV mixing process in its purist form.

## 2.2. Discretization

The model is vertically discretized using the grid shown in Fig. 2, with vorticity and divergence defined on 19 integer levels and pressure defined on the associated half-integer levels (Hsu and Arakawa 1990). The top boundary is assumed to be both an isentropic and isobaric surface, with  $\theta_T = 360$  K and  $p_T = 106$  hPa. The lower boundary was assumed to be the isentropic surface  $\theta_B = 298$  K, along which the pressure is variable in  $(x, y, t)$ . The potential temperatures on the 19 integer levels are 298.5, 299.5, 300.5, 301.5, 303.0, 305.0, 307.0, 309.0, 311.0, 313.0, 315.0, 317.0, 319.5, 323.0, 327.5, 333.0, 339.5, 347.0, 355.5 K, which gives the finest vertical resolution in the lower troposphere where the most intense PV mixing occurs.

The horizontal discretization is based on a double Fourier pseudospectral method having  $384 \times 384$  equally spaced collocation points on a doubly periodic horizontal domain of size  $600 \text{ km} \times 600 \text{ km}$ , which results in a 1.56 km spacing between points. For quadratic nonlinearities, this grid gives  $128 \times 128$  alias-free modes. The use of this double Fourier pseudospectral method makes it a simple matter to invert the relations  $\nabla^2 \psi = \zeta$  and  $\nabla^2 \chi = \delta$  to obtain new values of the streamfunction  $\psi$  and the velocity potential  $\chi$  after new values of  $\zeta$  and  $\delta$  have been predicted from (2.3) and (2.4). During PV mixing there is a cascade of potential enstrophy to the highest resolved wavenumbers. To avoid spectral blocking, we have included the ordinary diffusion terms  $\nu \nabla^2 \zeta$ ,  $\nu \nabla^2 \delta$ , and  $\nu \nabla^2 \sigma$  on the respective right hand sides of (2.3), (2.4), and (2.8), with the value of the diffusion coefficient chosen to be  $\nu = 100 \text{ m}^2 \text{ s}^{-1}$ . This value of the diffusion coefficient results

in a  $1/e$  damping time of 93 minutes for all modes having total wavenumber 128.

A third order Adams-Bashforth explicit scheme (Durrant 1991) is used for the time discretization needed in (2.3), (2.4), and (2.8). Because this primitive equation model allows rapidly propagating Lamb waves and uses an explicit time differencing scheme, the CFL condition requires a rather small time step. The model simulations shown here used a time step of 1 s.

Since inertia-gravity waves can be generated during PV mixing, a sponge layer was used near the lateral boundaries to minimize the false reappearance of these waves in the interior region of the model. It should be noted that the strict material conservation relation (2.9) is compromised by the use of a sponge layer near the domain edge and by the addition of ordinary diffusion terms to the right hand sides of (2.3) and (2.8). However, experience with the model indicates that these nonconservative effects are so weak that, for practical purposes, we can consider (2.9) to be satisfied. More information on the discretizations used in the model can be found in Hendricks (2008).

## 2.3. Initial conditions

Because the model contains the three prognostic equations (2.3), (2.4), and (2.8), we must specify the three initial fields  $\zeta(x, y, \theta, 0)$ ,  $\delta(x, y, \theta, 0)$ , and  $\sigma(x, y, \theta, 0)$ . To reduce the amount of inertia-gravity wave activity, we have chosen  $\delta(x, y, \theta, 0) = 0$ , so that  $\chi(x, y, \theta, 0) = 0$  and the entire initial wind field is determined by  $\zeta(x, y, \theta, 0)$ , or equivalently  $\psi(x, y, \theta, 0)$ . Two different initial conditions on  $\zeta$  were chosen—one resulting in a thick PV tower and the other resulting in a thin PV tower. These initial conditions are three-dimensional generalizations of the two-dimensional vorticity rings used in Schubert et al. (1999). The inner region is the low vorticity eye, the middle region is the high vorticity eyewall, and the outer region is the low vorticity environment. Hurricanes have often been observed to have such hollow profiles (Kossin and Eastin 2001). Using polar coordinates with the origin located at the center of the model domain, the initial condition for the isentropic relative vorticity has the separable form  $\zeta(r, \phi, \theta, 0) = [\zeta_{\text{sym}}(r) + \zeta_{\text{pert}}(r, \phi)]\Theta(\theta)$ , where the radial structure of the axisymmetric part is given by

$$\zeta_{\text{sym}}(r) = \begin{cases} 0 & 0 \leq r \leq r_1 \\ \zeta_2 S\left(\frac{r_2-r}{r_2-r_1}\right) & r_1 \leq r \leq r_2 \\ \zeta_2 & r_2 \leq r \leq r_3, \\ \zeta_2 S\left(\frac{r-r_3}{r_4-r_3}\right) + \zeta_3 S\left(\frac{r_4-r}{r_4-r_3}\right) & r_3 \leq r \leq r_4 \\ \zeta_3 & r_4 \leq r \end{cases} \quad (2.10)$$

and the vertical structure is given by

$$\Theta(\theta) = \begin{cases} 1 & \theta_B \leq \theta \leq \theta_{\text{ref}} \\ \exp\left[-\frac{1}{2}\left(\frac{\theta-\theta_{\text{ref}}}{20 \text{ K}}\right)^2\right] & \theta_{\text{ref}} \leq \theta \leq \theta_T. \end{cases} \quad (2.11)$$

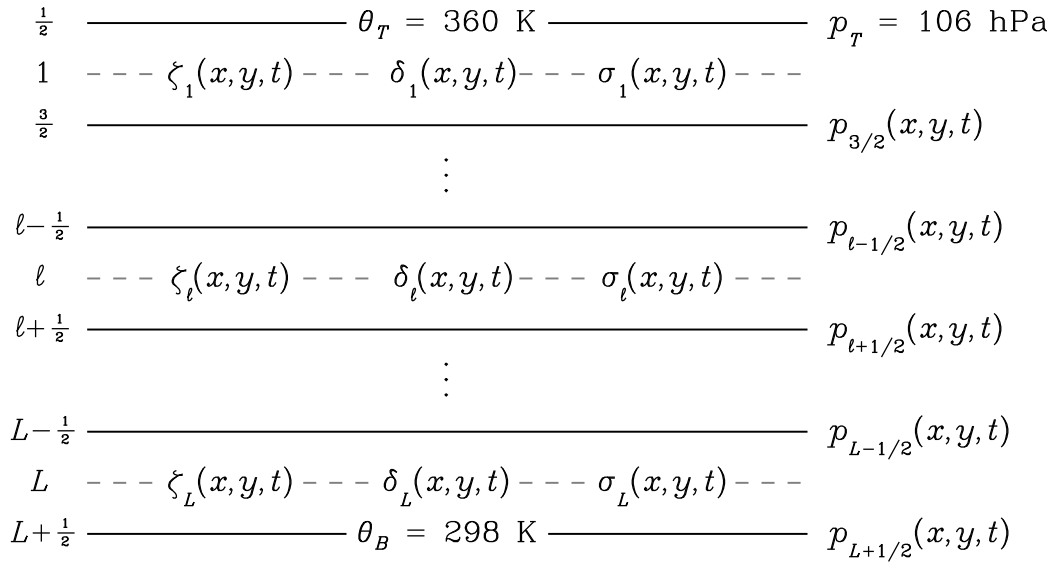


**Figure 2.** The vertical staggering of variables in the isentropic primitive equation model. The prognostic variables  $\zeta$ ,  $\delta$ ,  $\sigma$  are carried on the integer levels  $l = 1, 2, \dots, L$ , where we have chosen  $L = 19$ . Pressure is carried on the half-integer levels. The model top is assumed to be both an isentropic and an isobaric surface, with  $\theta_T = 360 \text{ K}$  and  $p_T = 106 \text{ hPa}$ . Pressure varies on the lower isentropic surface  $\theta_B = 298 \text{ K}$ .

Here,  $S(s) = 1 - 3s^2 + 2s^3$  is a cubic shape function that provides smooth transition zones, and  $\theta_{\text{ref}} = 302 \text{ K}$ . For the thick hollow tower,  $\zeta_2 = 0.0021 \text{ s}^{-1}$  and  $r_1, r_2, r_3, r_4 = 20, 24, 38, 42 \text{ km}$ , respectively. For the thin hollow tower,  $\zeta_2 = 0.0045 \text{ s}^{-1}$  and  $r_1, r_2, r_3, r_4 = 30, 34, 38, 42 \text{ km}$ , respectively. The average vorticity over  $0 \leq r \leq r_4$  is the same for both hollow towers, so that both vorticities have a maximum initial velocity of approximately  $30 \text{ m s}^{-1}$ . Because of the doubly periodic boundary conditions, the net circulation around the domain boundary vanishes on each isentropic surface, i.e., the horizontal average of the isentropic relative vorticity vanishes on each isentropic surface. Thus, after specification of  $r_1, r_2, r_3, r_4$  and  $\zeta_2$ , the constant  $\zeta_3$  is determined in such a way as to make the domain average of  $\zeta_{\text{sym}}(r)$  vanish. This leads to a value of  $\zeta_3$  that is negative, but its magnitude is small because the area outside  $r = r_4$  is approximately 64 times larger than the area inside  $r = r_4$ .

To initialize the  $\sigma$  field we first solve the isentropic coordinate version of the nonlinear balance equation as a two-dimensional Poisson equation for  $M$ , i.e.,

$$\nabla^2 M = 2 \left[ \frac{\partial^2 \psi}{\partial x^2} \frac{\partial^2 \psi}{\partial y^2} - \left( \frac{\partial^2 \psi}{\partial x \partial y} \right)^2 \right] + f \left( \frac{\partial^2 \psi}{\partial x^2} + \frac{\partial^2 \psi}{\partial y^2} \right), \quad (2.12)$$

where  $\psi$  is the streamfunction associated with the initial axisymmetric part of the vorticity field,  $\zeta_{\text{sym}}(r)\Theta(\theta)$ . The solution of (2.12), obtained at each integer level in the vertical, gives the initial  $M$  field to within an additive function

of  $\theta$ . This additive function was determined so that the horizontal area average of  $M$  over the  $600 \text{ km} \times 600 \text{ km}$  domain resulted in a vertical thermodynamic profile in agreement with the Jordan mean sounding. With  $M(x, y, \theta, 0)$  determined in this way, the  $\sigma(x, y, \theta, 0)$  can be obtained from  $\sigma = -(p/\kappa\Pi)(\partial^2 M/\partial\theta^2)$ , completing the initialization of the prognostic variables, except for the perturbation part of the vorticity, which was added to help initiate the instability process. This unbalanced, weak perturbation was added to the axisymmetric part of the vorticity at each isentropic level in the form

$$\zeta_{\text{pert}}(r, \phi) = \zeta_{\text{amp}} F(r) \sum_{n=1}^{12} \cos(n\phi + \varphi_n), \quad (2.13)$$

where

$$F(r) = \begin{cases} 0 & 0 \leq r \leq r_1, \\ S\left(\frac{r_2-r}{r_2-r_1}\right) & r_1 \leq r \leq r_2, \\ 1 & r_2 \leq r \leq r_3, \\ S\left(\frac{r-r_3}{r_4-r_3}\right) & r_3 \leq r \leq r_4, \\ 0 & r_4 \leq r, \end{cases} \quad (2.14)$$

$\zeta_{\text{amp}} = 1.0 \times 10^{-5} \text{ s}^{-1}$ , and  $\varphi_n$  is a random phase factor. This asymmetry in the initial vorticity, which mimics background noise associated with deep convection, is so weak that it is hardly detectable in the panels shown in Figs. 3 and 6.

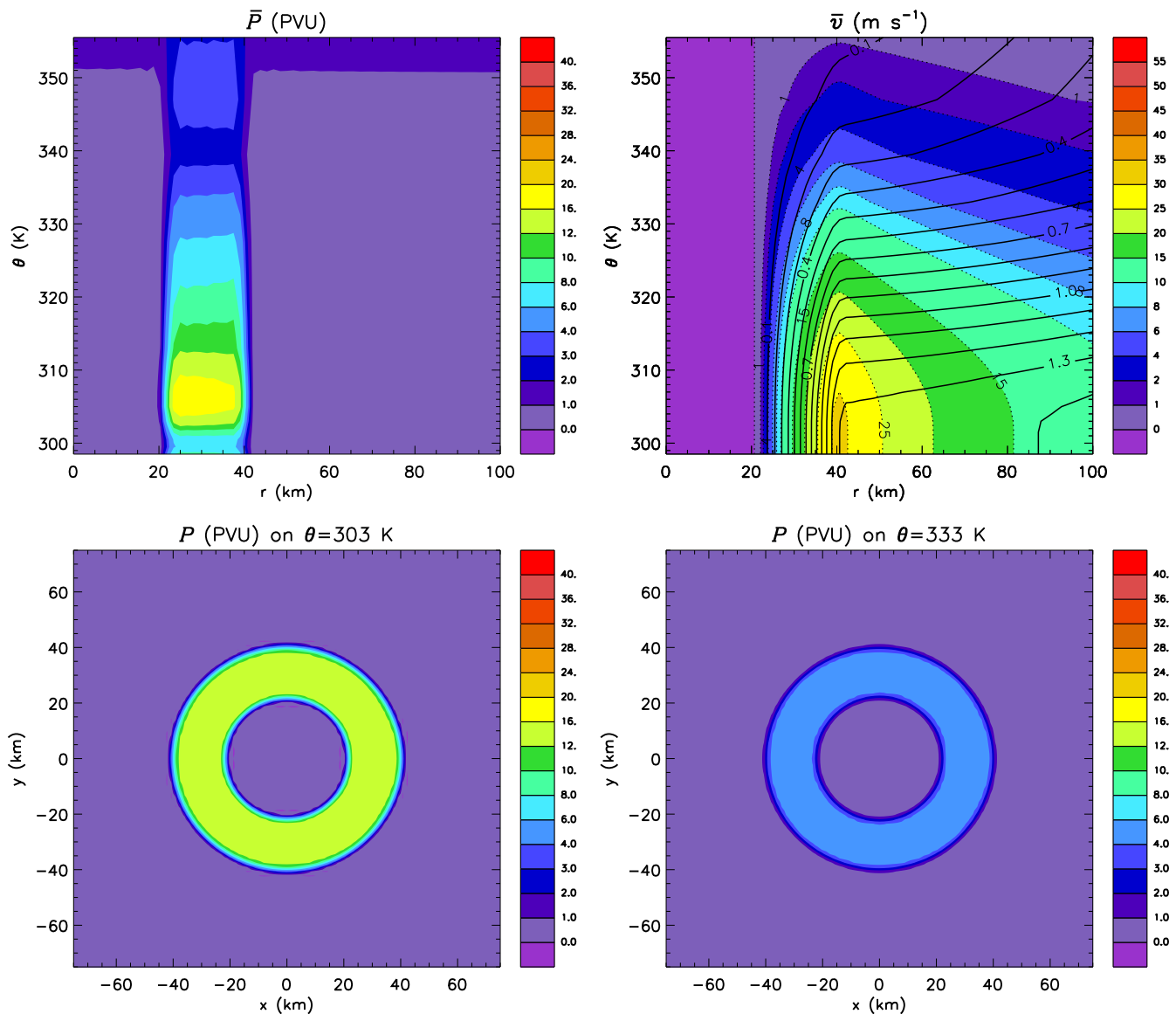


**Figure 3.** The initial condition for the thick PV hollow tower. Panels: azimuthal mean PV (top left), azimuthal mean tangential velocity with isosurfaces of normalized absolute angular momentum (top right), PV on the 303 K surface (bottom left), and PV on the 333 K surface (bottom right).

### 3. Nonlinear evolution of initially hollow PV structures

We now describe the evolution of the thick and thin PV towers over a 48 h period. The thick tower evolution is shown in Figs. 3–5, while the thin tower evolution is shown in Figs. 6–9. There are four panels in each figure. The top left panel is the azimuthal mean PV, the top right panel is the azimuthal mean tangential velocity (shaded) with contours of azimuthal mean absolute angular momentum (in units of  $10^6 \text{ m}^2 \text{ s}^{-1}$ ), the bottom left panel is the PV at the 303 K isentropic level (the 5th integer level from the surface), and the bottom right panel is the PV at the 333 K isentropic level (the 4th integer level from the top). We have chosen to present the output in the

model’s native  $\theta$ -coordinate. However, note that the geopotential varies on  $\theta$ -surfaces. In particular, at middle levels, the geopotential height of each  $\theta$ -surface is lower at the vortex center than at the boundaries, giving the vortex a warm-core. Potential vorticity magnitudes are expressed in potential vorticity units (PVU), where  $1 \text{ PVU} = 10^{-6} \text{ m}^2 \text{ K kg}^{-1} \text{ s}^{-1}$ .

Before discussing the nonlinear evolution of each hollow tower, it is first insightful to examine how small amplitude unstable PV waves grow in each layer. The linear stability analysis of Schubert et al. (1999) indicates that, in a barotropic context, the unstable vorticity wave growth rate is a function of the average inner-core vorticity, azimuthal wavenumber, the ring thickness, and the ring hollowness (i.e., the ratio of eye vorticity to average inner-core vorticity). Generally, the

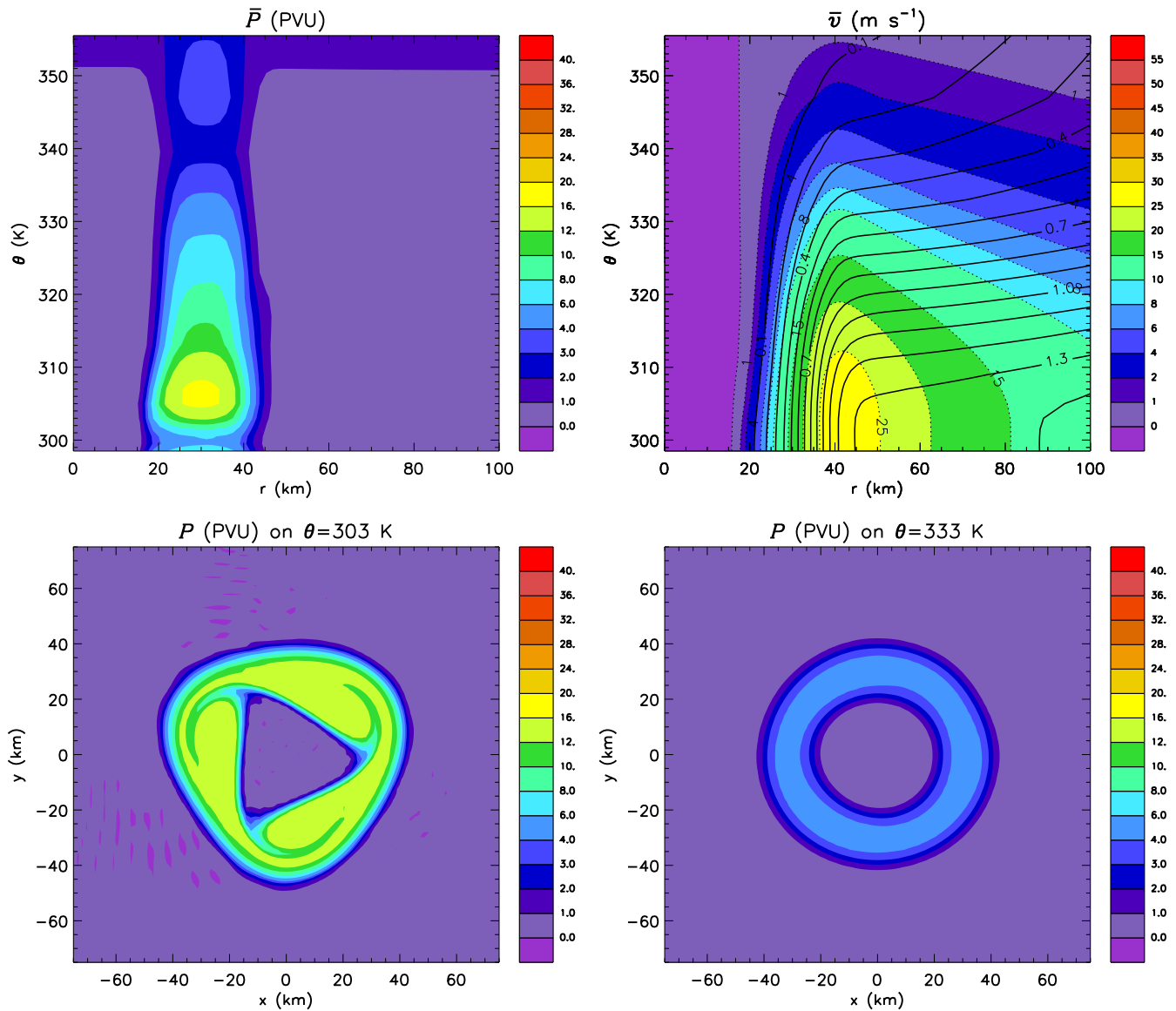


**Figure 4.** As in Fig. 3, but at  $t = 8$  h.

largest growth rates occur for disturbances on thinner and hollow rings, and there is also a tendency for the most unstable mode to be at a higher azimuthal wavenumber (see also Fig. 2 of Hendricks et al. 2009). We expect these barotropic results to be an adequate general guide to the present hollow PV towers, only in this case unstable PV waves may grow on PV rings in different isentropic layers. An important finding from Schubert et al. (1999) was that unstable wave growth rates were directly proportional to the average inner-core (eye and eyewall) vorticity. As we shall see, this will have a profound effect on determining the spatial distribution of PV at 48 h: the rearrangement of PV rings near the surface will occur more rapidly than at middle levels because the vorticity (and radial shear of the tangential wind) is larger there.

The thick hollow tower was constructed with a thickness

parameter  $\delta = (r_1 + r_2)/(r_3 + r_4) = 0.55$ . Based on the linear stability analysis, this vortex is most unstable to wavenumber  $n = 3$  in each isentropic layer, with  $e$ -folding times of 1.4 h at the surface and 3.7 h at  $\theta = 330$  K, respectively. Note that  $e$ -folding times were calculated using the Schubert et al. (1999) growth rate equation with the average inner-core vorticity in the isentropic layer. The thin hollow tower was constructed with a thickness of  $\delta = 0.80$ . This vortex is most unstable to wavenumber  $n = 5$  in each isentropic layer, with  $e$ -folding times of 0.3 h at the surface and 0.9 h at  $\theta = 330$  K, respectively. As stated earlier, there also exists a more intricate Rossby-inertia-gravity wave instability in these baroclinic vortices. However this instability is very sensitive to diffusive damping (Hodyss and Nolan 2008); for the diffusivity of  $\nu = 100 \text{ m}^2 \text{ s}^{-1}$  used in these experiments, we would not

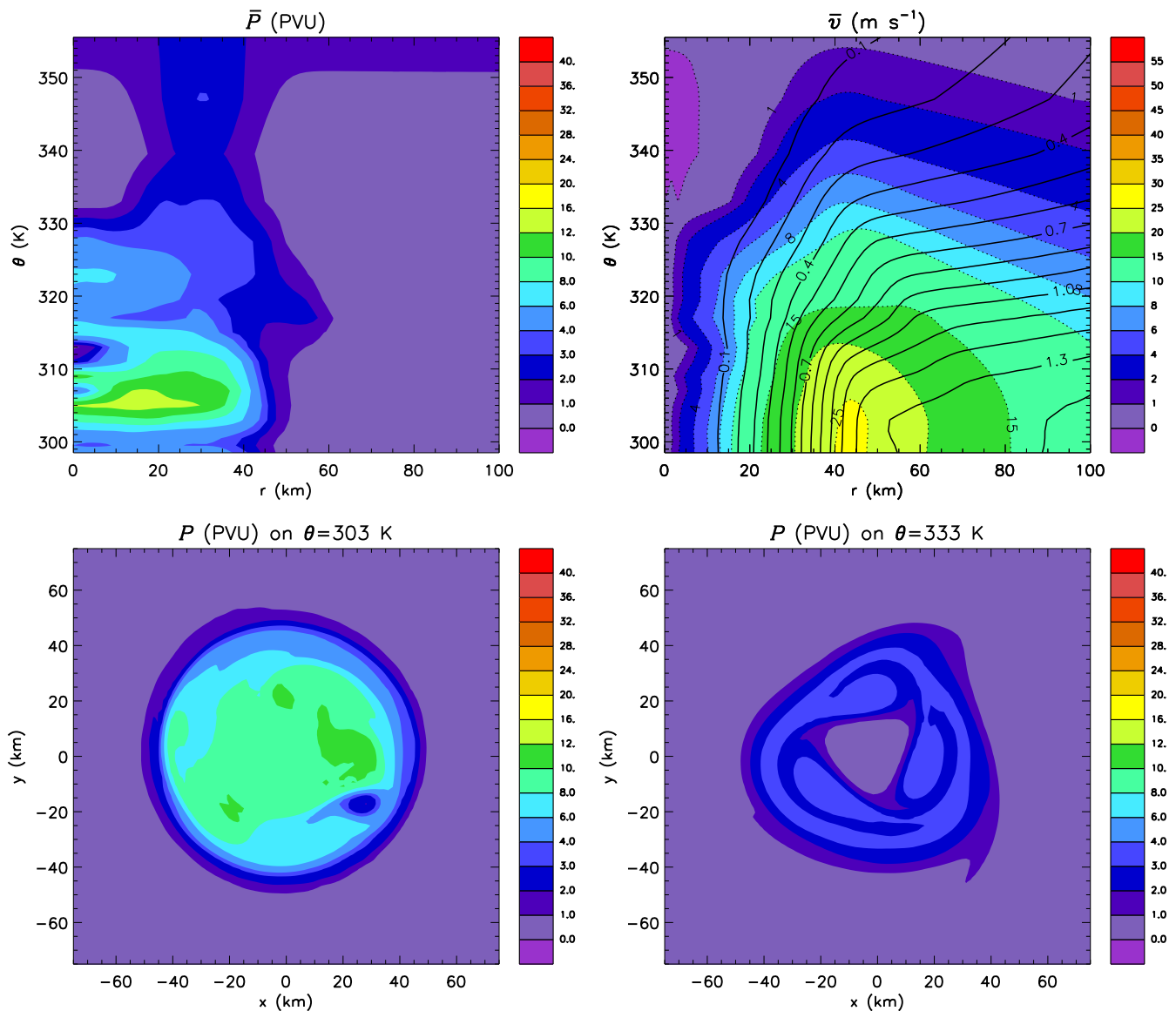


**Figure 5.** As in Fig. 3, but at  $t = 48$  h.

expect this instability to be important for PV wave growth. Finally, the existence of vertical shear in the vortex allows for the possibility of a combined barotropic-baroclinic instability, with disturbance PV tilting against both the horizontal and vertical shear of the tangential wind. Since the vertical shear of the tangential wind in these vortices (and, in nature) is much smaller than the radial shear, we expect that the instability will be mostly barotropic in nature (cf. Nolan and Montgomery 2002).

### 3.1. Thick hollow tower

The initial condition for the thick hollow tower is shown in Fig. 3. The PV is concentrated in the radial zone of cyclonic shear and curvature vorticity between  $r = 20$  and  $r = 40$  km, and is maximized at 305 K, even though the vortex winds are

maximum and equal from the surface to 302 K, before decaying above 302 K. PV is maximized at 305 K because of the balanced pseudodensity field, which has increased static stability above the surface. As we will soon see, unstable PV wave growth rates will be largest at this level, causing enhanced PV mixing there, and forming a PV bridge across the eye. In the bottom two panels of Fig. 3, horizontal slices of PV are shown at  $\theta = 303$  K and  $\theta = 333$  K. Note that rather thick PV rings are evident at both these levels, with larger PV near the surface.

Figure 4 shows the unforced evolution of the thick hollow tower at  $t = 8$  h. At this time, the most unstable wavenumber  $n = 3$  is visible. As the inner PV wave breaks cyclonically, PV becomes pooled into three regions, and low PV air from the eye is drawn into the eyewall in the form of filaments. As this PV ring begins to break down, the PV tower begins to shift in-

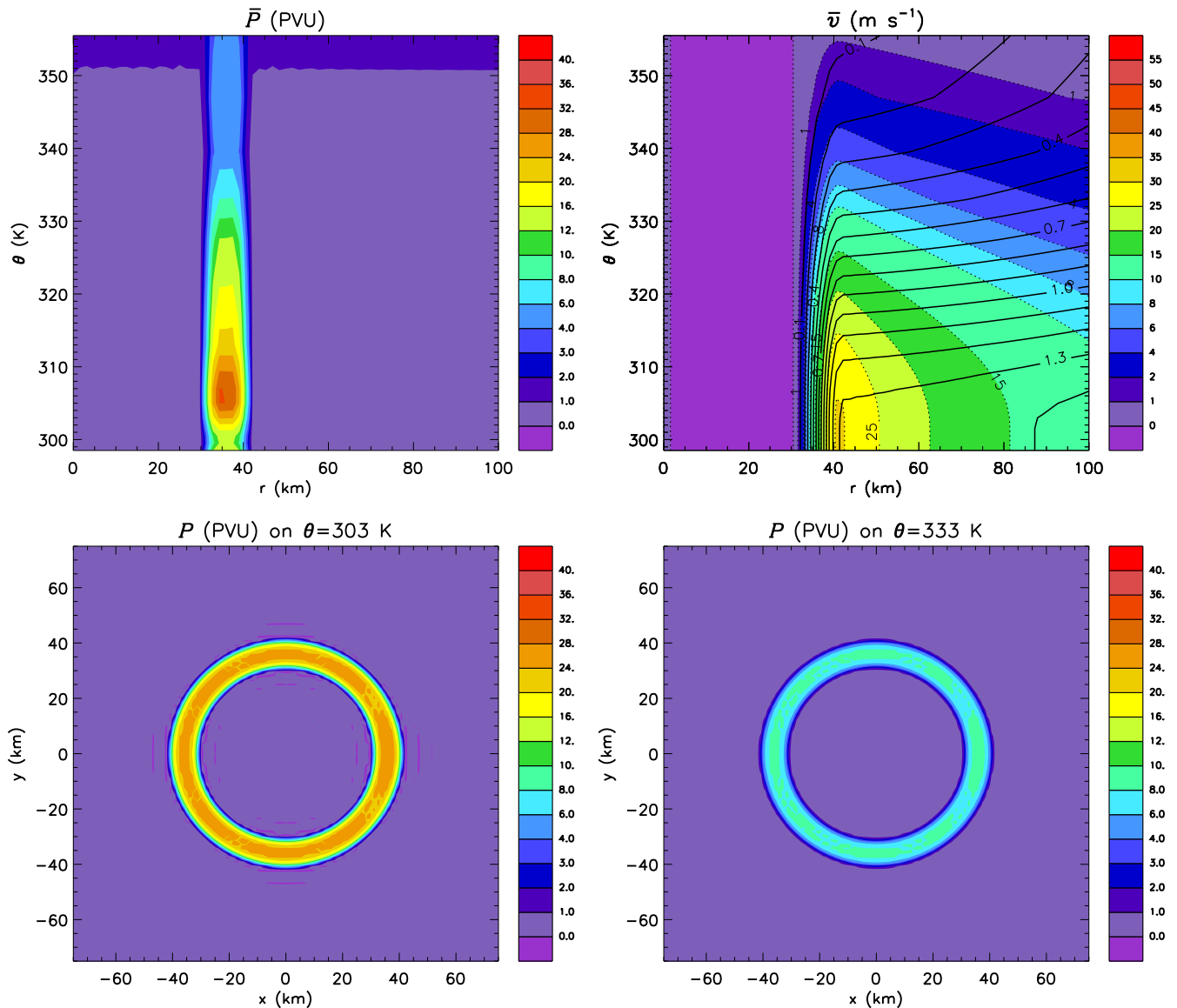


**Figure 6.** The initial condition for the thin PV hollow tower. Panels: azimuthal mean PV (top left), azimuthal mean tangential velocity with isosurfaces of normalized absolute angular momentum (top right), PV on the 303 K surface (bottom left), and PV on the 333 K surface (bottom right).

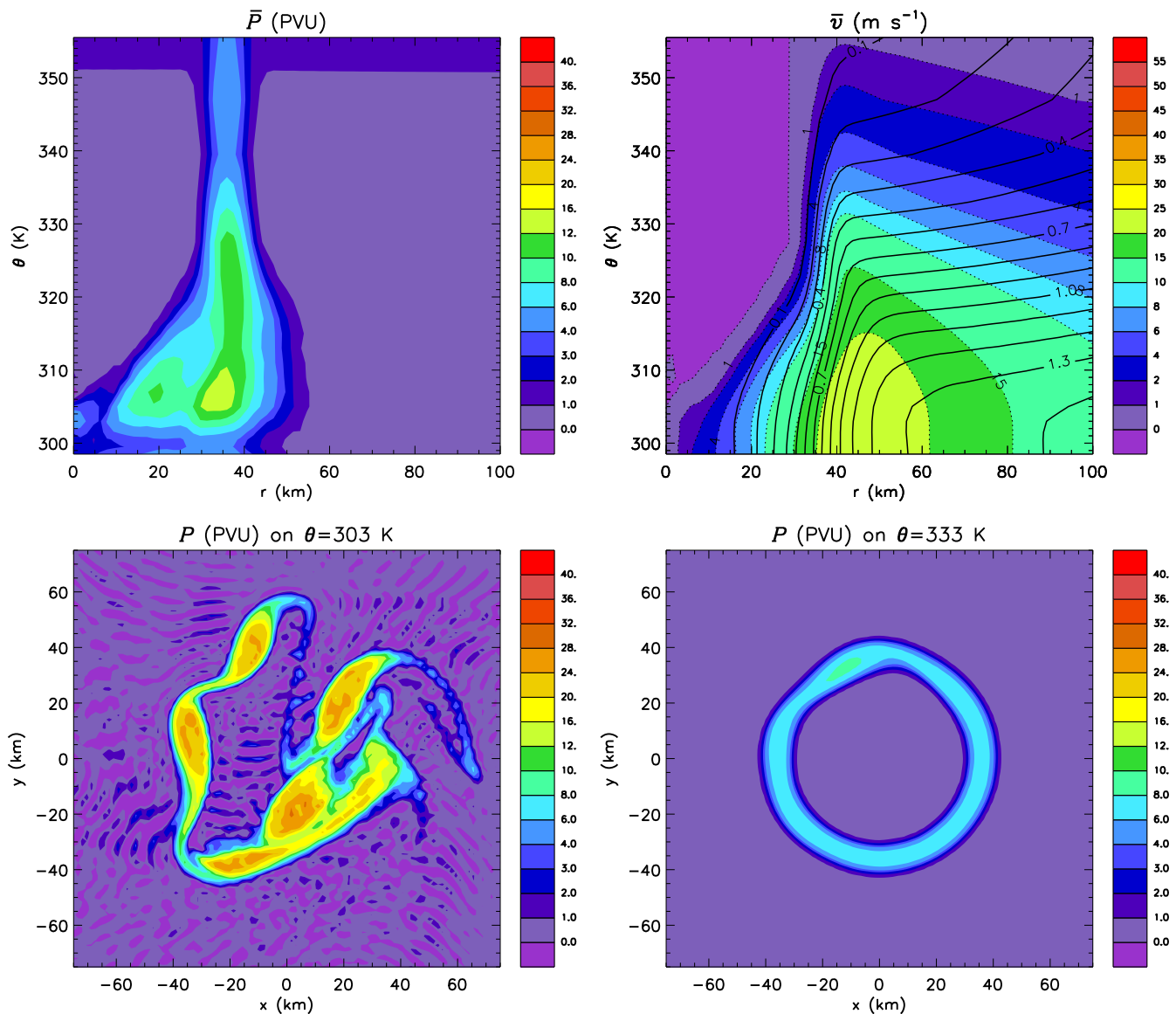
ward at low levels (see the top left panel of Fig. 4). In response to the PV at lower levels starting to be mixed into the eye, the absolute angular momentum surfaces begin to shift inward at lower levels. At this time, the middle level PV ring is still nearly annular, although a hint of a slower growing wavenumber 3 mode is evident.

Figure 5 shows the evolution at  $t = 48$  h. At this time, the low level PV ring has nearly symmetrized to a monopole, while the upper level ring is beginning to break down at azimuthal wavenumber 3. The result of the PV mixing during previous hours is evident in the azimuthal mean PV and tangential velocity plots (top panels). A bridge of high PV now crosses the eye at approximately  $\theta = 305$  K, and significant PV mixing between the eyewall and eye has occurred in the

interval  $298.5 \leq \theta \leq 332$  K. Above  $\theta = 332$  K, PV rings are just beginning to break down, but mixing has not yet occurred between the eyewall and eye. In response to preferential mixing at lower levels, the azimuthal mean tangential velocity has increased in the eye. Note also that iso-surfaces of absolute angular momentum now tilt outward with increasing height over the depth of the troposphere.

### 3.2. Thin hollow tower

The initial condition for the thin PV tower is shown in Fig. 6. Note that in this case the maximum PV is larger (28 PVU), and the radial zone of cyclonic shear and curvature vorticity is narrower. In the bottom two panels, the low and middle



**Figure 7.** As in Fig. 6, but at  $t = 4$  h.

level PV rings are shown. Note that the PV rings are quite thin and that the low level PV ring is more intense.

Figure 7 shows the evolution of thin hollow tower at  $t = 4$  h. At this time the low level PV ring has become most unstable to an azimuthal wavenumber-5 PV wave and has rolled up into multiple mesovortices. At this time, the upper level PV ring is still annular, although a hint of a slower growing PV wave is evident. Figure 8 shows the evolution of the thin hollow tower at  $t = 12$  h. At this time the low level mesovortices have rapidly merged into a monopole. Because of the progression of the instability on the middle level PV ring, it has now broken down into five mesovortices. The instability progresses more slowly at middle levels because the average inner-core PV at this level is smaller. In response to the rapid PV mixing at lower levels, a rather prominent PV bridge has

formed across the eye, and the entire PV tower now tilts outward from lower to upper levels. A significant spin-up of the low level outer eye has already occurred in response to the lower tropospheric PV mixing, and angular momentum surfaces tilt outward with increasing height.

Figure 9 shows the evolution of the thin hollow tower at  $t = 48$  h. At this time, both the low and middle level PV rings have symmetrized into monopoles (bottom panels). The azimuthal mean PV now has monopolar radial profiles from the surface to  $\theta = 345$  K, indicating that PV mixing has occurred between the eye and eyewall over a large portion of the troposphere. The PV bridge that formed earlier still exists across the eye at  $\theta = 305$  K. The azimuthal mean tangential velocity is similar to what it was at  $t = 12$  h, but spin-up has now also occurred at middle levels as the midlevel PV rings rolled up

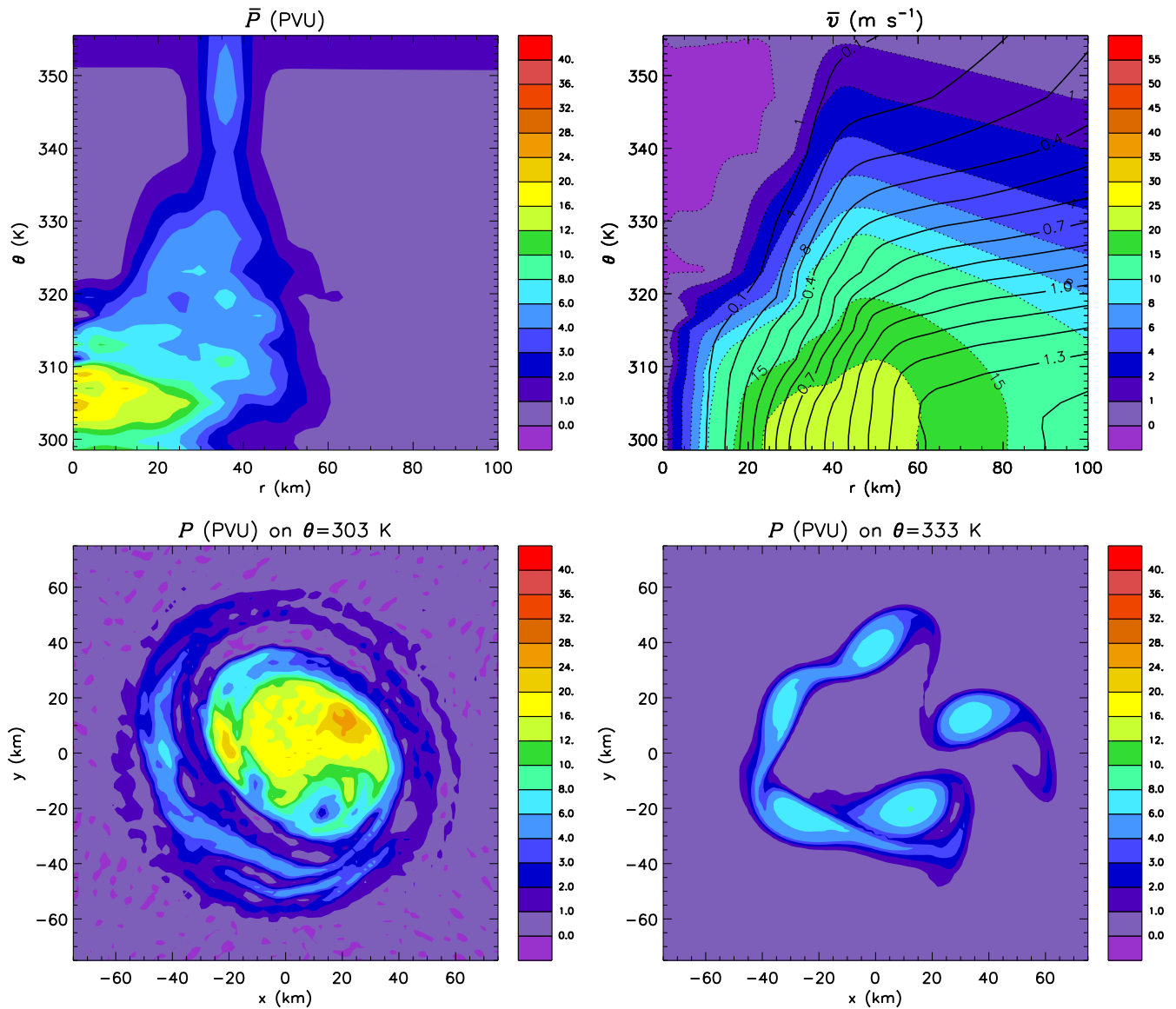


**Figure 8.** As in Fig. 6, but at  $t = 12$  h.

into mesovortices, which, after persisting for approximately 18 h, finally merged into a monopole.

### 3.3. Vortex intensity change

The change in maximum azimuthal mean azimuthal velocity ( $\bar{v}_{\text{max}}$ ) and minimum surface pressure ( $p_{\text{min}}$ ) were examined for each hollow tower. The thick tower had an initial intensity of  $\bar{v}_{\text{max}} = 30.9 \text{ m s}^{-1}$  and  $p_{\text{min}} = 1001.3 \text{ hPa}$ . At  $t = 48$  h, the new values were  $\bar{v}_{\text{max}} = 26.3 \text{ m s}^{-1}$  and  $p_{\text{min}} = 998.0 \text{ hPa}$ , or changes of  $-4.6 \text{ m s}^{-1}$  and  $-3.3 \text{ hPa}$ , respectively. The thin PV tower had an initial intensity of  $\bar{v}_{\text{max}} = 30.5 \text{ m s}^{-1}$  and  $p_{\text{min}} = 1002.7 \text{ hPa}$ . At  $t = 48$  h, the new values were  $\bar{v}_{\text{max}} = 23.5 \text{ m s}^{-1}$  and  $p_{\text{min}} = 997.2 \text{ hPa}$ , or changes of  $-7.0 \text{ m s}^{-1}$  and  $-5.5 \text{ hPa}$ , respectively. Note that the environmental surface pressure is approximately 1013 hPa.

For both hollow towers the maximum azimuthal mean azimuthal velocity and minimum central pressure decreased in tandem during PV mixing, and the decreases were most pronounced for the breakdown of the thin hollow tower. These results are consistent with the barotropic findings of Kossin and Schubert (2001) and Hendricks et al. (2009). The simultaneous decreases of minimum pressure and maximum wind present conflicting viewpoints of TC intensification. By minimum central pressure, both vortices intensified, but by maximum wind, both vortices weakened. However, these results are consistent with the final gradient and hydrostatically balanced states. The lower central pressures are due to the combined effects of the larger centrifugal term and warmer air (see next subsection) at middle levels in new balanced mass and wind configurations of the final PV fields. In any event,

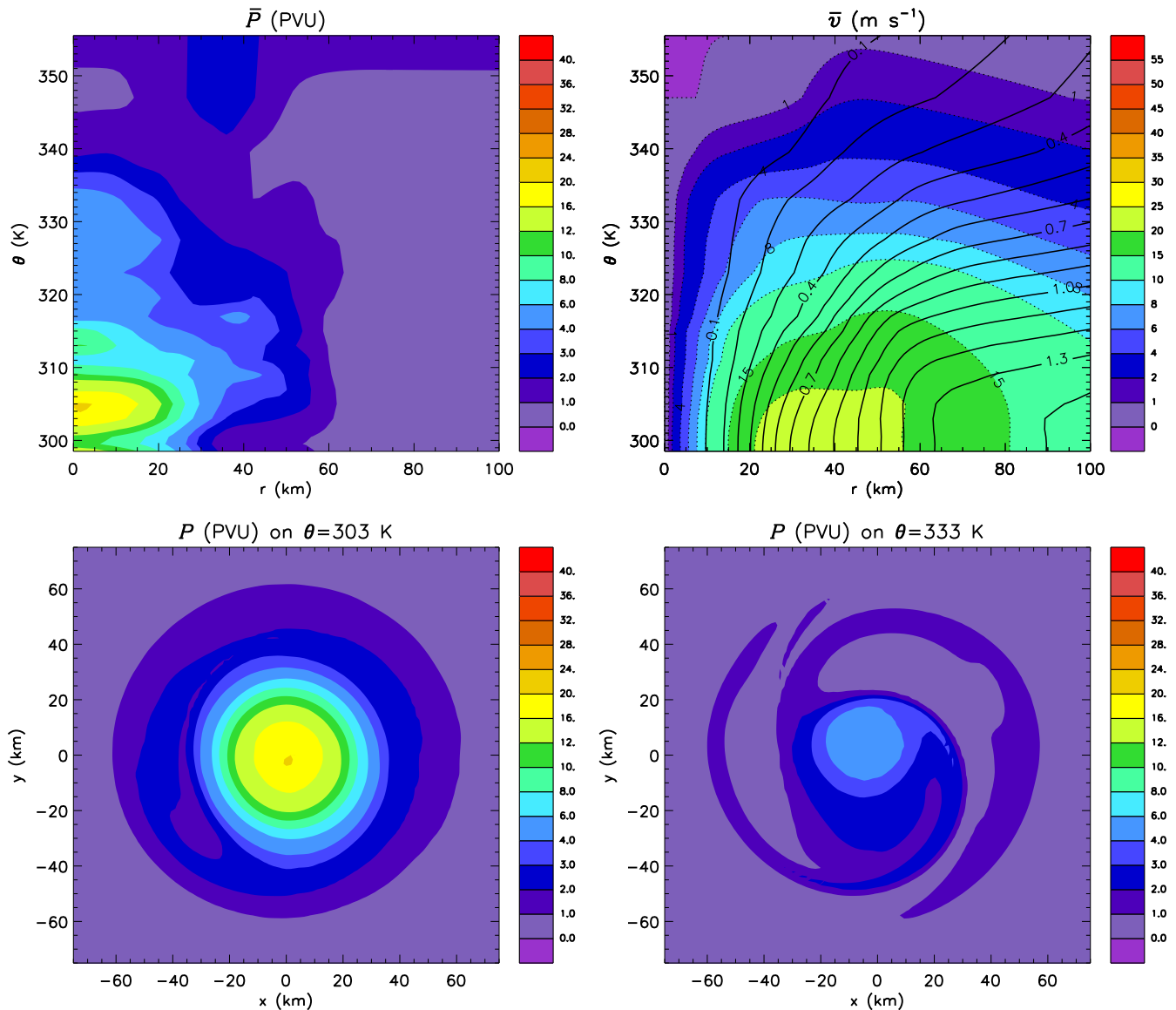


**Figure 9.** As in Fig. 6, but at  $t = 48$  h.

these results indicate that large pressure falls can happen during the breakdown of thin three-dimensional hollow towers in an adiabatic framework.

### 3.4. Eye vertical profiles

At lower levels, observed hurricane eyes typically have a temperature inversion that separates the moist cloudy air below from the clear dry air above (Jordan 1952, Willoughby 1998). The height of the inversion can vary but typically it is near 850 hPa. Figure 10 shows two examples of this inversion structure, taken from eye soundings in Hurricanes Jimena (1991) and Olivia (1994). The profile for Jimena is more characteristic of an intensifying tropical cyclone, while the profile for Olivia is more characteristic of a steady-state or weakening tropical cyclone (Willoughby 1998). Note that a sharp inversion (ap-

proximately 3 K) exists near 850 hPa for Jimena. As a consequence of PV mixing between the eyewall and eye, significant structural change has been shown to occur for both the thick and thin PV towers in our idealized simulations. In this subsection, we explore the idea that the hurricane eye temperature inversion discussed above may be at least partially under the dynamical control of the PV mixing process.

When potential vorticity is advected in a quasi-balanced flow, the invertibility principle indicates that new balanced wind and mass fields quickly adjust to support the new PV distribution. At any given time and spatial point, the PV can be considered to be the product of two factors: the isentropic absolute vorticity ( $f + \zeta$ ) and the static stability  $-g(\partial\theta/\partial p)$ . The latter factor becomes large when  $\theta$  surfaces are packed together tightly in the vertical. Solution of the invertibility prin-

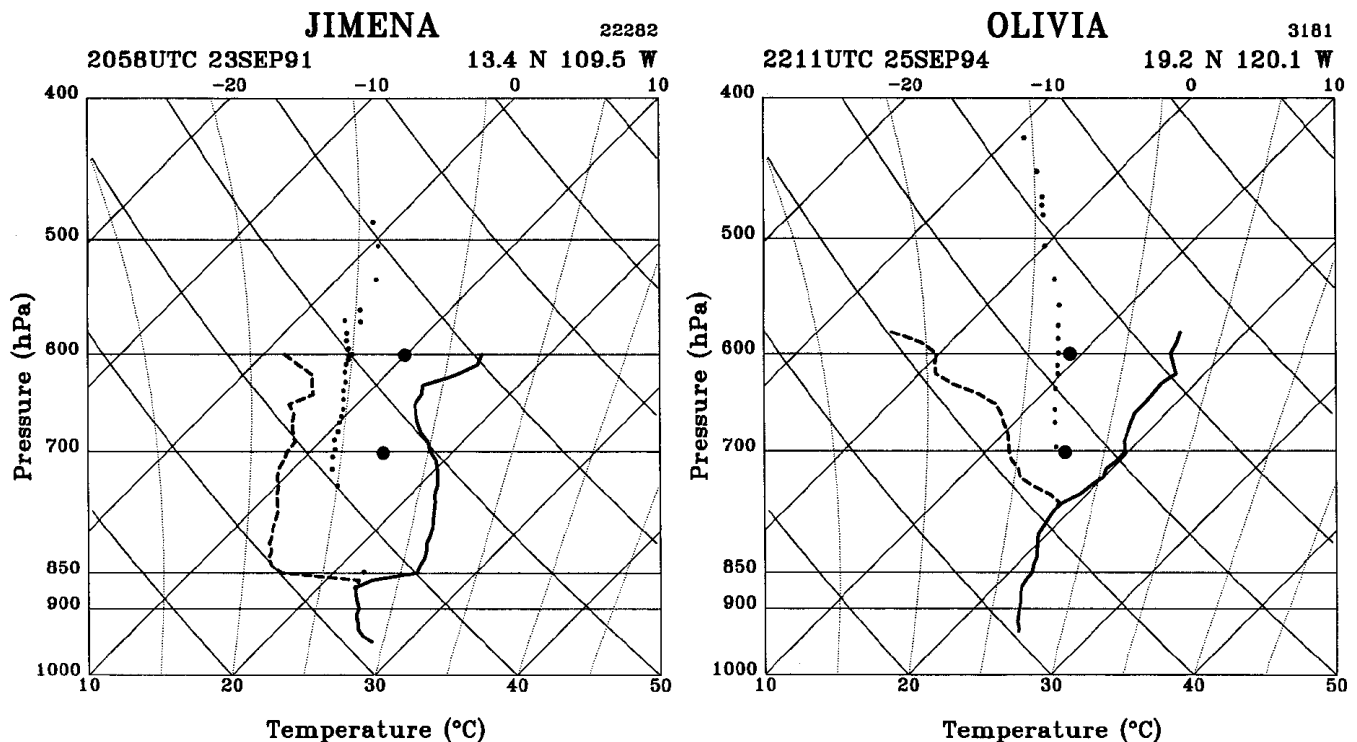


**Figure 10.** Observed eye soundings in Hurricanes Jimena (1991) and Olivia (1994). Reproduced from Willoughby (1998).

ciple can then be viewed as a mathematical procedure that partitions the PV at each point into its two factors ( $f + \zeta$ ) and  $-g(\partial\theta/\partial p)$ . Thus, when the PV mixing process enhances the PV at low levels in the eye, we should expect this local PV increase to show up as simultaneous increases in both the isentropic absolute vorticity ( $f + \zeta$ ) and the static stability  $-g(\partial\theta/\partial p)$ . In this sense, the mixing of high PV into the core at low levels can result in high static stability there, i.e., there is the possibility of a dynamically induced inversion, as opposed to a thermodynamically induced inversion.

Figure 11 shows vertical temperature profiles in the eye, before and after PV mixing for the thick and thin hollow towers. For both towers, the balanced mass field after PV mixing yielded warming from approximately 950 to 700 hPa. The thick tower exhibited peak warming of approximately 3 K at 850 hPa, while the thin tower exhibited peak warming of 6 K at 850 hPa. In both cases, weak inversions formed near this level. The location of these inversions is consistent with observations of many hurricanes (Willoughby 1998). However, in real hurricanes the thermally indirect transverse circulation associated with eyewall diabatic heating induces eye warming through subsidence, a process that has been neglected in the adiabatic model runs presented here. Thus, the model results shown here indicate that PV mixing complements diabatic processes, and thus help explain why observed eye temperature inversions near 850 hPa are so strong. Based on observations, Willoughby (1998) found that hurricanes with strong eye temperature inversions were typically intensifying while hurricanes with weaker temperature inversions were steady or

weakening. Since we have documented that both large pressure falls and significant warming at 850 hPa can result from PV mixing, the existence of a strong hurricane eye inversion signifies a deepening central pressure via this internal mixing mechanism.

## 4. Azimuthal mean diagnostics

In this section, angular momentum budgets are performed to assess the relative roles of mean and eddy processes in the change of angular momentum due to PV mixing. Since it has been shown in the previous section that the adiabatic evolution of hollow towers is fundamentally an asymmetric process, we expect a dominant contribution from the eddy term to the total change in azimuthal mean angular momentum. The diagnostic analysis presented here is based on azimuthal averaging along isentropic surfaces, which leads to a compact and elegant form of wave-mean flow interaction theory (Andrews 1983, Tung 1986, Andrews et al. 1987).

### 4.1. Azimuthal mean equations

The cylindrical coordinate versions of equations (2.1), (2.2), (2.7), and (2.8) are

$$\frac{\partial u}{\partial t} - \sigma P v + \frac{\partial}{\partial r} \left[ M + \frac{1}{2}(u^2 + v^2) \right] = 0, \quad (4.1)$$

$$\frac{\partial v}{\partial t} + \sigma P u + \frac{\partial}{r \partial \phi} \left[ M + \frac{1}{2}(u^2 + v^2) \right] = 0, \quad (4.2)$$

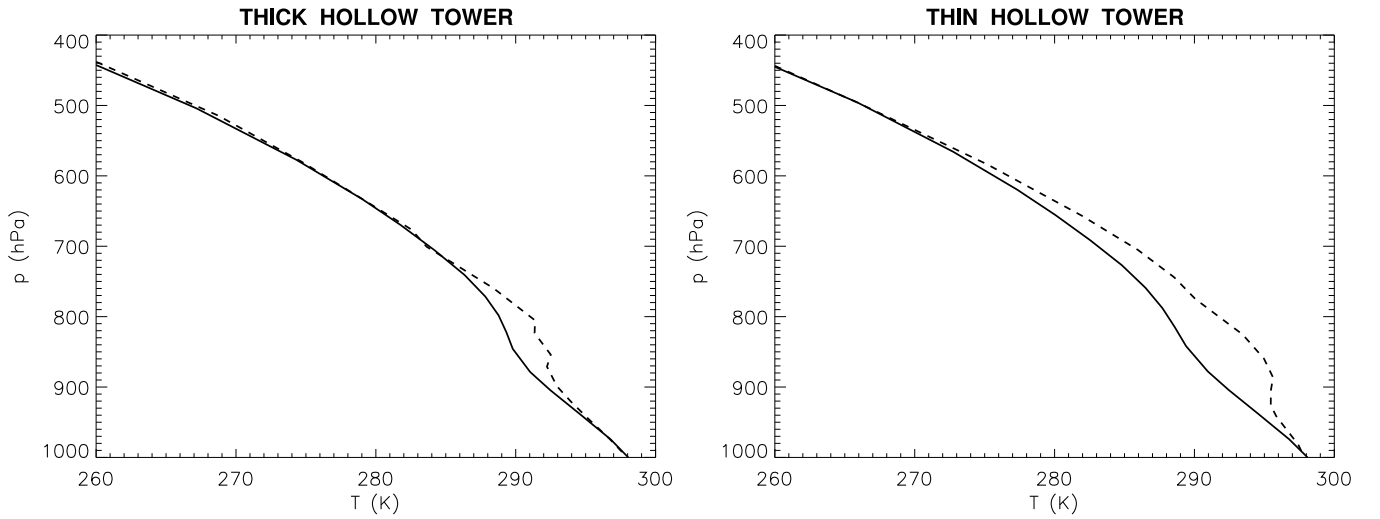


**Figure 11.** Eye vertical temperature profiles at  $t = 0$  h (solid curve; before PV mixing), and at  $t = 48$  h (dashed curve; after PV mixing) for the thick (left panel) and thin (right panel) hollow towers.

$$\frac{\partial M}{\partial \theta} - \Pi = 0, \quad (4.3)$$

$$\frac{\partial \sigma}{\partial t} + \frac{\partial(r\sigma u)}{r\partial r} + \frac{\partial(\sigma v)}{r\partial \phi} = 0, \quad (4.4)$$

where  $u$  and  $v$  are now the radial and azimuthal velocity components, and where, for the simplified diagnostic analysis presented here, we have continued to neglect any nonconservative effects on the right hand sides of (4.1), (4.2), and (4.4). To derive the azimuthal mean equations from (4.1)–(4.4) we shall define two types of azimuthal average—an ordinary average on an isentropic surface and a mass-weighted average on an isentropic surface. For example, the ordinary azimuthal average of  $v$  is defined by

$$\bar{v}(r, \theta, t) = \frac{1}{2\pi} \int_0^{2\pi} v(r, \phi, \theta, t) d\phi. \quad (4.5)$$

For the radial wind  $u$ , the mass-weighted azimuthal average is defined by  $\hat{u} = \overline{\sigma u} / \bar{\sigma}$ . The deviation from the ordinary average is defined by  $v' = v - \bar{v}$ , and the deviation from the mass-weighted average is defined by  $u^* = u - \hat{u}$ . Similar definitions hold for the other variables.

Applying  $\overline{(\quad)}$  to each term in (4.4) and noting that  $\overline{\sigma u} = \bar{\sigma} \hat{u}$ , we can write the azimuthal mean mass continuity equation as

$$\frac{\partial \bar{\sigma}}{\partial t} + \frac{\partial(r\bar{\sigma}\hat{u})}{r\partial r} = 0. \quad (4.6)$$

Similarly, applying  $\overline{(\quad)}$  to each term in (4.2) and noting that  $\overline{\sigma P u} = \bar{\sigma} \hat{P} \hat{u} + \overline{\sigma P^* u^*}$  we can write the azimuthal mean  $v$  equation as

$$\frac{\partial \bar{v}}{\partial t} + (f + \bar{\zeta}) \hat{u} = -\overline{\sigma P^* u^*}. \quad (4.7)$$

Equations (4.6) and (4.7) can also be written in the advective forms (4.13) and (4.11), where  $\mathcal{D}/\mathcal{D}t$  and  $\mathcal{G}$  are defined in (4.14) and (4.16).

Now consider the radial momentum equation. Since both (4.6) and (4.7) contain  $\hat{u}$ , we would like to transform (4.1) into a prediction equation for  $\hat{u}$ . This requires putting (4.1) into a flux form before taking the azimuthal average. Thus, combining (4.1) and (4.4), we obtain the flux form

$$\begin{aligned} \frac{\partial(\sigma u)}{\partial t} + \frac{\partial(r\sigma u u)}{r\partial r} + \frac{\partial(\sigma v u)}{r\partial \phi} \\ - \left(f + \frac{v}{r}\right) \sigma v + \sigma \frac{\partial M}{\partial r} = 0. \end{aligned} \quad (4.8)$$

Taking the azimuthal average of (4.8), we obtain

$$\frac{\partial(\overline{\sigma u})}{\partial t} + \frac{\partial(r\overline{\sigma u u})}{r\partial r} - \overline{\left(f + \frac{v}{r}\right) \sigma v} + \overline{\sigma \frac{\partial M}{\partial r}} = 0. \quad (4.9)$$

Noting that  $\overline{\sigma u} = \bar{\sigma} \hat{u}$ ,  $\overline{\sigma u u} = \bar{\sigma} \hat{u} \hat{u} + \overline{\sigma u^* u^*}$ ,  $\overline{\sigma(\partial M/\partial r)} = \bar{\sigma}(\partial \bar{M}/\partial r) + \overline{\sigma'(\partial M'/\partial r)}$ , and using the azimuthal mean continuity equation (4.6), we obtain the advective form (4.10).

Collecting the above results, and taking the azimuthal average of (4.3), we obtain the complete set of azimuthal mean equations

$$\frac{\mathcal{D}\hat{u}}{\mathcal{D}t} - \left(f + \frac{\bar{v}}{r}\right) \bar{v} + \frac{\partial \bar{M}}{\partial r} = \mathcal{F}, \quad (4.10)$$

$$\frac{\mathcal{D}\bar{m}}{\mathcal{D}t} = r\mathcal{G}, \quad (4.11)$$

$$\frac{\partial \bar{M}}{\partial \theta} - \Pi(\bar{p}) = \overline{\Pi(p)} - \Pi(\bar{p}), \quad (4.12)$$

$$\frac{\mathcal{D}\bar{\sigma}}{\mathcal{D}t} + \bar{\sigma} \frac{\partial(r\hat{u})}{r\partial r} = 0, \quad (4.13)$$

where

$$\frac{\mathcal{D}}{\mathcal{D}t} = \frac{\partial}{\partial t} + \hat{u} \frac{\partial}{\partial r} \quad (4.14)$$

is the azimuthal mean material derivative,  $\bar{m} = r\bar{v} + \frac{1}{2}f r^2$  is the azimuthal mean absolute angular momentum, and where

$$\mathcal{F} = -\frac{1}{\bar{\sigma}} \left[ \frac{\partial(\overline{r\sigma u^* u^*})}{r\partial r} - \left( f + \frac{\bar{v}}{r} \right) \overline{\sigma' v'} - \frac{(\overline{\sigma v})' v'}{r} + \overline{\sigma' \frac{\partial M'}{\partial r}} \right] \quad (4.15)$$

and

$$\mathcal{G} = -\overline{\sigma P^* u^*} \quad (4.16)$$

are the eddy-induced effective mean radial and azimuthal forces per unit mass. Equations (4.10)–(4.13) have the form of the axisymmetric primitive equations for  $\hat{u}$ ,  $\bar{v}$ ,  $\bar{M}$ ,  $\bar{p}$ , all of which are functions of  $(r, \theta, t)$ . The terms  $\mathcal{F}$ ,  $\mathcal{G}$ , and  $\overline{\Pi(\bar{p})} - \Pi(\bar{p})$  appear as forcings. Note that  $\overline{\Pi(\bar{p})}$  is computed by taking the azimuthal average after raising  $p$  to the  $\kappa$  power, while  $\Pi(\bar{p})$  is computed by reversing the order of these two operations. According to (4.11), the azimuthal mean absolute angular momentum is “materially conserved” in the absence of the eddy torque term  $r\mathcal{G}$ , which will turn out to be the most important forcing term in the azimuthal mean equations.

As discussed in the appendix, it is possible to express the torque  $r\mathcal{G}$  in terms of the pseudodivergence of the Eliassen-Palm flux, i.e.,

$$r\bar{\sigma} \overline{\sigma P^* u^*} = \frac{\partial[\overline{r(\sigma u)' m'}]}{r\partial r} + \frac{\partial[-(\bar{p}'/g)(\partial M'/\partial \phi)]}{\partial \theta} + \frac{\partial[\overline{\sigma' m'}]}{\partial t}. \quad (4.17)$$

One possible way to perform a diagnostic analysis of the wave-mean flow interaction is to plot an E-P cross-section, i.e., to plot the Eliassen-Palm flux vector, with radial component  $\overline{(\sigma u)' m'}$  and vertical component  $-\bar{p}'(\partial M'/\partial \phi)$ , and its divergence in the  $(r, \theta)$ -plane. An advantage of this procedure is that the tilt of the Eliassen-Palm flux vector in the  $(r, \theta)$ -plane indicates the relative importance of the barotropic process  $\overline{(\sigma u)' m'}$  and the baroclinic process  $-\bar{p}'(\partial M'/\partial \phi)$ . However, the compact form of  $\mathcal{G}$  given in (4.16) is well-suited for our present analysis.

## 4.2. Balanced model

In the primitive equation model simulations presented here the azimuthal mean vortex remains close to a state of gradient balance, so that the azimuthal mean primitive equation model (4.10)–(4.13) is well-approximated by the balanced vortex model. The usefulness of the balanced vortex model is that it provides a clearer understanding of how the density-weighted azimuthal mean radial velocity  $\hat{u}$  is induced by the eddy PV flux  $\overline{\sigma P^* u^*}$ . Sufficient conditions for the validity of the balanced vortex approximation are that  $|\mathcal{F}|$  remains small compared to the pressure gradient and Coriolis/centrifugal

terms and that the forcing term  $\mathcal{G}$  has a slow enough time scale that significant, azimuthal mean inertia-gravity waves are not excited, i.e.,  $|\mathcal{D}\hat{u}/\mathcal{D}t|$  also remains small compared to the pressure gradient and Coriolis/centrifugal terms. Under these conditions, the azimuthal mean primitive equations reduce to the azimuthal mean balance equations

$$\left( f + \frac{\bar{v}}{r} \right) \bar{v} = \frac{\partial \bar{M}}{\partial r}, \quad (4.18)$$

$$\frac{\partial \bar{v}}{\partial t} - \hat{P} \frac{\partial \Psi}{\partial \theta} = \mathcal{G}, \quad (4.19)$$

$$\frac{\partial \bar{M}}{\partial \theta} = \Pi(\bar{p}), \quad (4.20)$$

$$\frac{\partial \Pi(\bar{p})}{\partial t} + g\Gamma(\bar{p}) \frac{\partial(r\Psi)}{r\partial r} = 0, \quad (4.21)$$

where  $\Gamma(\bar{p}) = d\Pi(\bar{p})/d\bar{p} = \kappa\Pi(\bar{p})/\bar{p}$ , and where we have used the azimuthal mean continuity equation (4.6) to introduce the streamfunction  $\Psi$  such that

$$\left( -\frac{1}{g} \frac{\partial \bar{p}}{\partial t}, \bar{\sigma} \hat{u} \right) = \left( \frac{\partial(r\Psi)}{r\partial r}, -\frac{\partial \Psi}{\partial \theta} \right). \quad (4.22)$$

Taking the time derivative of (4.18) and (4.20), and then eliminating  $\partial \bar{M}/\partial t$  between the resulting two equations, we obtain

$$\frac{\partial}{\partial \theta} \left( \bar{f} \frac{\partial \bar{v}}{\partial t} \right) = \frac{\partial}{\partial r} \left( \frac{\partial \Pi(\bar{p})}{\partial t} \right), \quad (4.23)$$

where  $\bar{f} = f + 2\bar{v}/r$ . Substituting from (4.19) for  $\partial \bar{v}/\partial t$  and from (4.21) for  $\partial \Pi(\bar{p})/\partial t$ , (4.23) becomes

$$\frac{\partial}{\partial r} \left( g\Gamma \frac{\partial(r\Psi)}{r\partial r} \right) + \frac{\partial}{\partial \theta} \left( \bar{f} \hat{P} \frac{\partial \Psi}{\partial \theta} \right) = -\frac{\partial(\bar{f}\mathcal{G})}{\partial \theta}. \quad (4.24)$$

Since  $\Gamma > 0$  and  $\bar{f}\hat{P} > 0$  everywhere, (4.24) is a second order elliptic equation for  $\Psi$  when  $\mathcal{G}$  is known. Thus, in the context of the gradient balance approximation, the streamfunction  $\Psi$  is determined by the instantaneous structure of the azimuthal mean vortex through the terms  $\bar{f}$ ,  $\hat{P}$ ,  $\Gamma(\bar{p})$ , and by the instantaneous structure of the azimuthal mean eddy PV flux through the term  $\partial(\bar{f}\mathcal{G})/\partial \theta$ . In this sense, the azimuthal mean radial mass flux  $\bar{\sigma}\hat{u}$  and the time rate of change of the azimuthal mean pressure on isentropic surfaces  $\partial \bar{p}/\partial t$  are determined by  $\mathcal{G}$  through (4.24) and (4.22). For given  $\bar{f}$ ,  $\hat{P}$ ,  $\Gamma(\bar{p})$ ,  $\mathcal{G}$  fields, the resulting unique  $\bar{\sigma}\hat{u}$  and  $\partial \bar{p}/\partial t$  fields are those that result in a continuing state of thermal wind balance.

## 4.3. Absolute angular momentum budgets

Absolute angular momentum budgets were computed for the evolution of each PV tower. Equation (4.7) was first re-written as

$$\frac{\partial \bar{m}}{\partial t} = -(f + \bar{\zeta})r\hat{u} - \overline{r\sigma P^* u^*}, \quad (4.25)$$

where the first term on the right hand side is the mean term and the second term is the eddy term. The left hand side is the actual tendency of absolute angular momentum. Equation

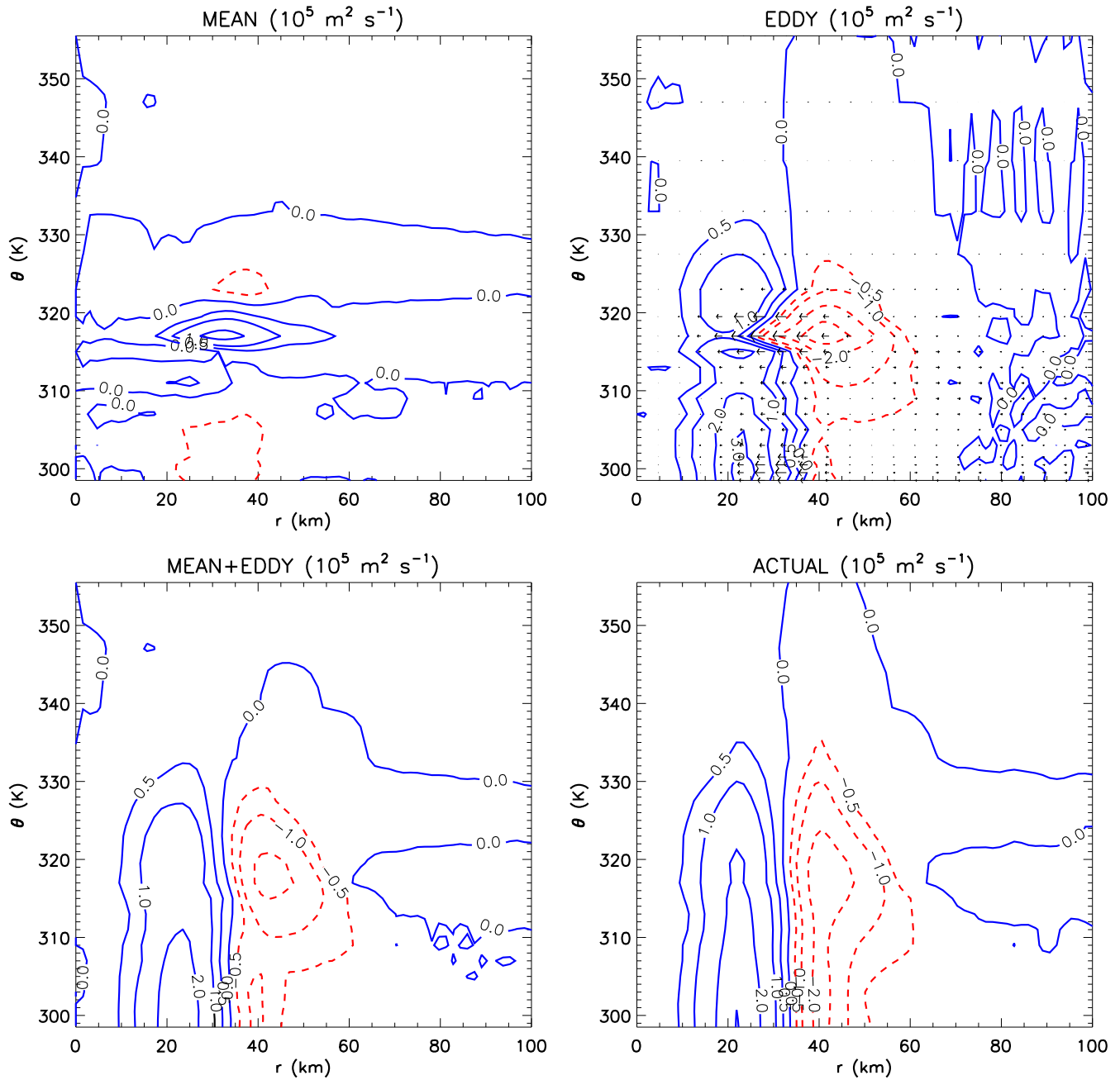


**Figure 12.** Absolute angular momentum budget from  $t = 0$  to  $t = 48$  h for the thick hollow tower. The upper left panel is the time integral of the mean term  $-(f + \tilde{\zeta})r\bar{u}$  and the upper right panel is the time integral of the eddy term  $r\mathcal{G} = -r\overline{\sigma P^* u^*}$ . The lower left panel is the sum of the mean and eddy terms, i.e., the time integral of  $-(f + \tilde{\zeta})r\bar{u} + r\mathcal{G}$ . The lower right panel is the time integral of the actual model tendency  $\partial\bar{v}/\partial t$ . In the top right panel, the radial component of the Eliassen-Palm flux vectors are overlaid, with a vector plotted on every third radial grid point. In all four panels, isolines greater than or equal to zero are solid blue, while isolines less than zero are dashed red.

(4.25) was integrated over 48 hours using the trapezoidal rule on 15 minute resolution model output to obtain net changes in the azimuthal mean angular momentum induced by each term.

The angular momentum budgets for the thick and thin hollow towers are presented in Figs. 12 and 13, respectively.

In each figure, the top left and right panels are the time integrals of the mean and eddy terms, respectively. The bottom left panel is the sum of the mean and eddy terms, and the bottom right panel is the actual change in absolute angular momentum observed in the numerical simulation over 48 h. The bottom right and bottom left panels should be similar, ac-

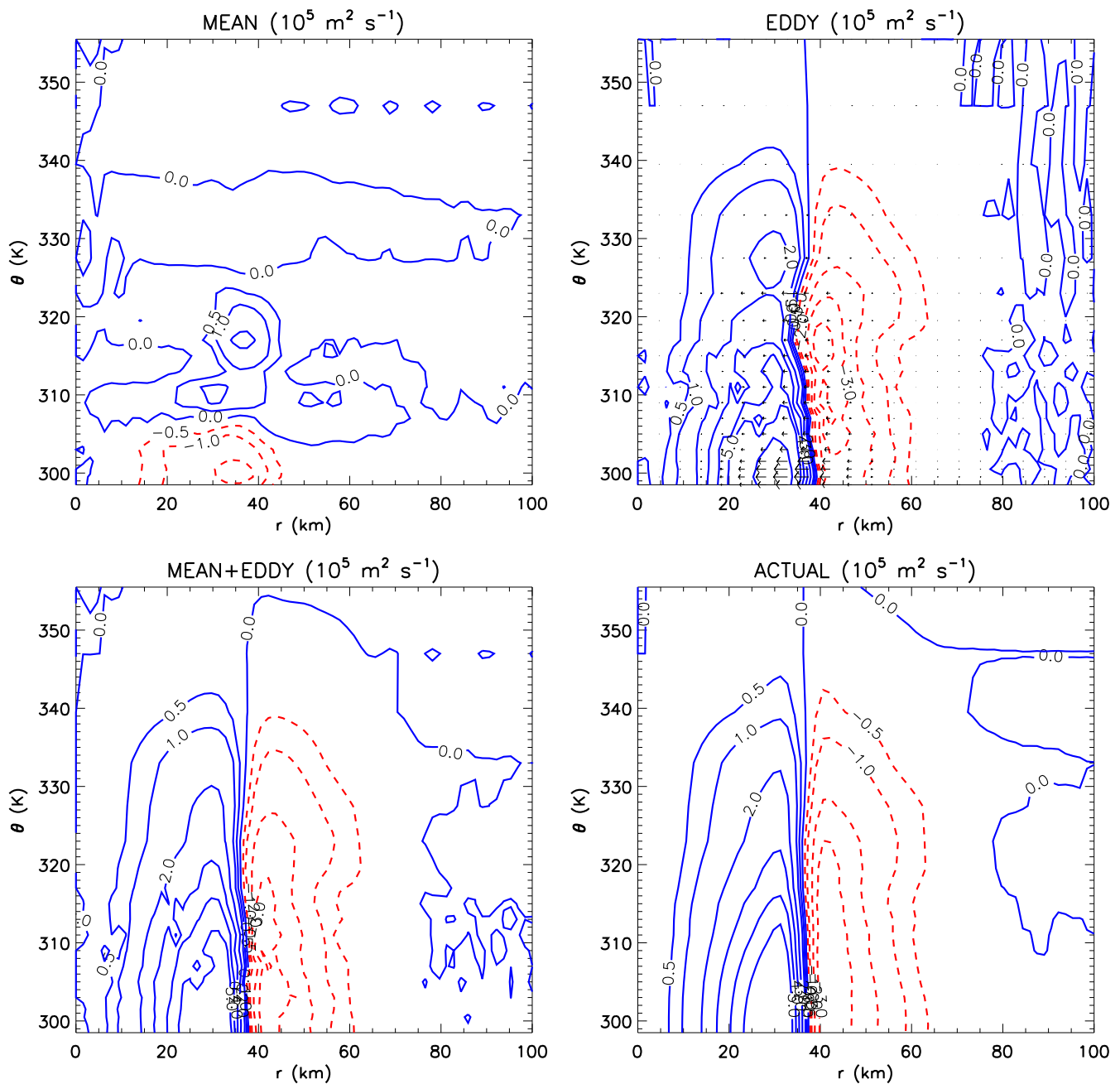


**Figure 13.** Same as Fig. 12, but for the thin hollow tower.

ording to (4.25); however, they will not match perfectly because of the existence of diffusion and the lateral sponge layer in the model simulations, as well as the 15 minute time discretization. In the top right panels the radial component of the Eliassen-Palm flux vectors, integrated from  $t = 0$  to  $t = 48$  h, are overlaid. The vertical components were found to be very small in comparison to the radial components, indicating that the wave-mean flow interaction here is primarily barotropic in nature.

Beginning with the thick hollow tower, in the top left panel of Fig. 12 it can be seen that the mean term is small

nearly everywhere in the  $(r, \theta)$  plane. The most significant contribution is at  $r = 30$  km and  $\theta = 318$  K. The eddy term, on the other hand (top right panel) shows a spin-down in the region  $30 \leq r \leq 50$  km and  $310 \leq \theta \leq 330$  K, and a spin-up in the region  $10 \leq r \leq 30$  km and  $299 \leq \theta \leq 330$  K. The summation of the mean and eddy terms is shown in the bottom left panel, and it compares favorably with the actual change in absolute angular momentum (bottom right panel).

A similar budget is evident for the thin hollow tower (Fig. 13). The mean term is small as well, with the most dominant contribution near  $r = 35$  km and  $\theta = 318$  K. However,

there is a more pronounced spin-down at  $r = 35$  km and  $\theta = 302$  K. The eddy term for the thin tower exhibits similar behavior to the thick tower, with a spin-down in the region  $40 \leq r \leq 60$  km and  $299 \leq \theta \leq 335$  K, and spin-up in the region  $10 \leq r \leq 40$  km and  $299 \leq \theta \leq 335$  K. The addition of the mean and eddy terms is shown in the bottom left panel, and it compares favorably with the actual change in absolute angular momentum during PV mixing (bottom right panel). The main differences between this budget and the thick tower budget is that the magnitudes of the terms are larger.

As discussed in Section 4.1, the wave-mean flow interaction may also be viewed as the divergence of the Eliassen-Palm flux vector, with the radial and vertical components associated with contributions by barotropic and baroclinic processes, respectively. Note that in the top right panels of Figs. 12 and 13, the Eliassen-Palm flux vectors point radially inward in the region of strongest PV mixing. Also note that the vectors are converging where the time average of  $\overline{\sigma P^* u^*}$  is positive, and diverging where the time average of  $\overline{\sigma P^* u^*}$  is negative. Thus, the wave-mean flow interaction here can also be viewed as resulting from these radial eddy angular momentum flux divergences. In a sense, adiabatic PV mixing in the two continuously stratified examples shown here can be viewed as the summation of barotropic PV mixing in individual isentropic layers, with PV anomalies in different isentropic layers only weakly interacting with one another.

The absolute angular momentum budgets indicate that the eddy term is dominant in the spin-down of the vortex just outside the radius of maximum wind of the initial hollow towers and the spin-up of the vortex inside the radius of maximum wind. This conclusively shows that PV mixing between the eye and eyewall is an eddy-driven asymmetric process that is important for vortex structural and intensity change.

The results presented here generally support the insightful angular momentum budget arguments made by Malkus (1958), who pointed out that "one of the most amazing features of hurricane eyes is their weak surface winds." Her arguments emphasize the importance of the turbulent incorporation of high angular momentum air from the eyewall into the eye. Although her analysis was made before the widespread use of numerical models and before the development of the wave-mean flow interaction theory used in Section 4, her approach and our approach are consistent and complementary in the sense that our approach emphasizes the role of the PV flux  $\overline{\sigma P^* u^*}$ , while her approach emphasizes the role of the angular momentum flux  $(\overline{\sigma u})' m'$ . The connection between these two fluxes and their importance to the angular momentum budget can be seen through (4.7) and (4.17).

## 5. Conclusions

Diabatic heating in the eyewall of hurricanes produces and maintains an annular hollow tower of PV from the surface to the middle troposphere. However, if the hollow tower is thin enough, it may break down, causing the diabatically produced

PV in the eyewall to be mixed into the eye, which leads to significant vortex structural and intensity change. In this paper, we have examined the nonlinear evolution of such hollow tower structures in an idealized, quasi-conservative framework. Two prototypical hurricane-like hollow towers (one thick and one thin) were constructed, and their unforced evolution was examined in a primitive equation model with an isentropic vertical coordinate.

The primary results of this study are as follows:

- The balanced mass field resulting from PV mixing between the eyewall and eye yields temperatures that are warmer between 900 and 700 hPa (with peak warming of approximately 3-6 K near 850 hPa), so that weak temperature inversions can form. Thus, in certain instances, the observed hurricane eye inversion can be partially dynamically controlled by PV mixing on isentropic surfaces. Since the vortex minimum pressure falls in response to PV mixing, the existence of a strong eye inversion is a signal of a deepening tropical cyclone via this internal mixing mechanism.
- Absolute angular momentum surfaces that are initially oriented vertically tilt in response to PV mixing that occurs preferentially at lower levels. Since the observed hurricane eyewall is an absolute angular momentum surface above the boundary layer (Stern and Nolan 2009), these results indicate an adiabatic theory for the formation of the hurricane eyewall tilt.
- A dynamical explanation for a PV bridge across the hurricane eye has been proposed. Typical hurricane-like vortices have a hollow profile with a PV maximum just above the surface. Unstable PV waves grow most rapidly at low levels, where the radial shear of the tangential wind and curvature vorticity are largest, causing PV to be mixed into the eye most rapidly there. Since the initial PV is maximized above the surface, this causes a PV bridge to form across the eye.
- During PV mixing events in these idealized three-dimensional vortices, the minimum central pressure and maximum mean tangential velocity both decrease. Rapid pressure falls were found to occur during the break down of the thin hollow tower, thus PV mixing may complement the vortex intensification process. Absolute angular momentum budgets indicate that the eddy-induced radially inward PV flux term is dominant in spinning up the vortex from the surface to middle levels inside the initial radius of maximum wind.
- While low level eye mesovortices have been shown to exist observationally and in barotropic model simulations, these results indicate that long-lived mid-level mesovortices may also exist in the hurricane eye. The mesovortices exist for long times at middle levels because unstable PV wave growth rates are significantly

smaller there. Since there is typically no airborne cloud-water at mid-levels, such mesovortices would be difficult to observe remotely; however it would be interesting to examine flight level data to see if mesovortex signatures exist there.

In closing, we wish to emphasize that the dry adiabatic framework used here to examine PV mixing here is an oversimplification of the real atmosphere. The PV structure in real hurricanes is also influenced by nonconservative effects of moist diabatic processes, surface friction, and vertical diffusion, which have been neglected in this study. In particular diabatic PV production would tend to accompany the inward mixing at low levels, and similarly diabatic PV destruction would likely accompany the outflow at middle to upper levels. Diabatic effects also create a secondary circulation (not present in our study) causing PV to be increased locally when there is vertical mass divergence and vice-versa. Future work should be focused on studying PV mixing in more complex scenarios. The present work could be extended by including surface friction effects and diabatic forcing to regenerate the PV hollow tower. In this light, it would be interesting to see if the combined effects of diabatic heating and friction can make hollow towers less susceptible to breakdown and mixing (Wu et al. 2009). Additionally it would be interesting to see how this intrinsic mixing process is affected by vertical wind shear and other environmental forcings. Finally, the process could be examined in more complex full-physics mesoscale models.

**Acknowledgments:** We would like to thank Rick Taft, Brian McNoldy, Scott Fulton, and two anonymous reviewers for their helpful comments. This research was performed in part while the first author held a National Research Council Research Associateship Award at the U.S. Naval Research Laboratory in Monterey, CA and while he was a PhD student at Colorado State University. The work of the second author has been supported by the National Science Foundation under Grants ATM-0837932 and ATM-0833032 and under the Science and Technology Center for Multi-Scale Modeling of Atmospheric Processes, managed by Colorado State University through cooperative agreement No. ATM-0425247. Model simulations were performed on high-end Linux workstations generously provided through a gift from the Hewlett-Packard Corporation.

## Appendix: Derivation of the Taylor relation

Following Tung (1986), the primitive equation form of the Taylor relation can be obtained by deriving an alternate form of the absolute angular momentum principle, followed by a comparison with the form (4.20). The alternate derivation of the absolute angular momentum principle begins by writing

(4.2) in the flux form

$$\frac{\partial(\sigma v)}{\partial t} + \frac{\partial(r^2 \sigma uv)}{r^2 \partial r} + \frac{\partial(\sigma v v)}{r \partial \phi} + f \sigma u + \sigma \frac{\partial M}{r \partial \phi} = 0, \quad (\text{A.1})$$

and then taking the azimuthal average to obtain

$$\frac{\partial(\overline{\sigma v})}{\partial t} + \frac{\partial(r^2 \overline{\sigma uv})}{r^2 \partial r} + f \overline{\sigma u} + \sigma \frac{\partial M}{r \partial \phi} = 0. \quad (\text{A.2})$$

The last term on the left hand side of (A.2) can be rewritten using

$$\sigma \frac{\partial M}{\partial \phi} = -\frac{\partial}{\partial \theta} \left( \frac{p}{g} \frac{\partial M}{\partial \phi} \right) + \frac{\partial}{g \partial \phi} \left\{ \int_0^p \kappa \Pi(p') dp' \right\}, \quad (\text{A.3})$$

the azimuthal average of which yields

$$\overline{\sigma \frac{\partial M}{\partial \phi}} = -\frac{\partial}{\partial \theta} \left( \frac{p}{g} \frac{\partial M}{\partial \phi} \right) = -\frac{\partial}{\partial \theta} \left( \frac{p'}{g} \frac{\partial M'}{\partial \phi} \right). \quad (\text{A.4})$$

Using (A.4) in (A.2) and noting that  $\overline{\sigma u} = \overline{\sigma} \bar{u}$  and  $\overline{\sigma v} = \overline{\sigma} \bar{v} + \overline{\sigma' v'}$ , we obtain

$$\begin{aligned} \frac{D\bar{m}}{Dt} = & -\frac{1}{\bar{\sigma}} \left\{ \frac{\partial[r(\sigma u)'m']}{r \partial r} \right. \\ & \left. + \frac{\partial[-(p'/g)(\partial M'/\partial \phi)]}{\partial \theta} + \frac{\partial[\overline{\sigma' m'}]}{\partial t} \right\}, \end{aligned} \quad (\text{A.5})$$

where  $m' = rv'$  and  $D/Dt$  is defined by (4.14). Since the left hand sides of (4.11) and (A.5) are identical, the right hand sides of these two equations must be equal, which results in the nonlinear Taylor relation (4.17).

## References

- Andrews, D. G., 1983: A finite-amplitude Eliassen-Palm theorem in isentropic coordinates. *J. Atmos. Sci.*, **40**, 1877–1883, doi: [10.1175/1520-0469\(1983\)040<1877:AFAEPT>2.0.CO;2](https://doi.org/10.1175/1520-0469(1983)040<1877:AFAEPT>2.0.CO;2).
- Andrews, D. G., J. R. Holton, and C. B. Leovy, 1987: Middle Atmosphere Dynamics. Academic Press, 489 pages.
- Bell, M. M., and M. T. Montgomery, 2008: Observed structure, evolution, and potential intensity of category 5 Hurricane Isabel (2003) from 12 to 14 September. *Mon. Wea. Rev.*, **136**, 2023–2046, doi: [10.1175/2007MWR1858.1](https://doi.org/10.1175/2007MWR1858.1).
- Durran, D. R., 1991: The third-order Adams-Bashforth method: An attractive alternative to leapfrog time differencing. *Mon. Wea. Rev.*, **119**, 702–720, doi: [10.1175/1520-0493\(1991\)119<0702:TTOABM>2.0.CO;2](https://doi.org/10.1175/1520-0493(1991)119<0702:TTOABM>2.0.CO;2).
- Eliassen, A., 1983: The Charney-Stern theorem on barotropic-baroclinic instability. *Pure Appl. Geophys.*, **121**, 563–572, doi: [10.1007/BF02590155](https://doi.org/10.1007/BF02590155).
- Guinn, T. A., 1992: A dynamical theory for hurricane spiral

- bands. Ph.D. Dissertation, Colorado State University, 178 pages.
- Hendricks, E. A., 2008: Tropical cyclone evolution via internal asymmetric dynamics. Ph.D. Dissertation, Colorado State University, 150 pages.
- Hendricks, E. A., W. H. Schubert, R. K. Taft, H. Wang, and J. P. Kossin, 2009: Lifecycles of hurricane-like vorticity rings. *J. Atmos. Sci.*, **66**, 705–722, doi: [10.1175/2008JAS2820.1](https://doi.org/10.1175/2008JAS2820.1).
- Hodyss, D., and D. S. Nolan, 2008: The Rossby-inertia-buoyancy instability in baroclinic vortices. *Phys. Fluids*, **20**, 096602, doi: [10.1063/1.2980354](https://doi.org/10.1063/1.2980354).
- Hoskins, B. J., M. E. McIntyre, and A. W. Robertson, 1985: On the use and significance of isentropic potential vorticity maps. *Quart. J. Roy. Meteor. Soc.*, **111**, 877–946, doi: [10.1002/qj.49711147002](https://doi.org/10.1002/qj.49711147002).
- Hsu, Y.-J. G., and A. Arakawa, 1990: Numerical modeling of the atmosphere with an isentropic vertical coordinate. *Mon. Wea. Rev.*, **118**, 1933–1959, doi: [10.1175/1520-0493\(1990\)118<1933:NMOTAW>2.0.CO;2](https://doi.org/10.1175/1520-0493(1990)118<1933:NMOTAW>2.0.CO;2).
- Jordan, C. L., 1952: On the low-level structure of the typhoon eye. *J. Meteor.*, **9**, 285–290.
- Kossin, J. P., and M. D. Eastin, 2001: Two distinct regimes in the kinematic and thermodynamic structure of the hurricane eye and eyewall. *J. Atmos. Sci.*, **58**, 1079–1090, doi: [10.1175/1520-0469\(2001\)058<1079:TDRITK>2.0.CO;2](https://doi.org/10.1175/1520-0469(2001)058<1079:TDRITK>2.0.CO;2).
- Kossin, J. P., and W. H. Schubert, 2001: Mesovortices, polygonal flow patterns, and rapid pressure falls in hurricane-like vortices. *J. Atmos. Sci.*, **58**, 2196–2209, doi: [10.1175/1520-0469\(2001\)058<2196:MPFPAR>2.0.CO;2](https://doi.org/10.1175/1520-0469(2001)058<2196:MPFPAR>2.0.CO;2).
- Kossin, J. P., B. D. McNoldy, and W. H. Schubert, 2002: Vortical swirls in hurricane eye clouds. *Mon. Wea. Rev.*, **130**, 3144–3149, doi: [10.1175/1520-0493\(2002\)130<3144:VSIHEC>2.0.CO;2](https://doi.org/10.1175/1520-0493(2002)130<3144:VSIHEC>2.0.CO;2).
- Kossin, J. P., and W. H. Schubert, 2004: Mesovortices in Hurricane Isabel. *Bull. Amer. Meteor. Soc.*, **85**, 151–153, doi: [10.1175/BAMS-85-2-151](https://doi.org/10.1175/BAMS-85-2-151).
- Malkus, J. S., 1958: On the structure and maintenance of the mature hurricane eye. *J. Meteor.*, **15**, 337–349.
- Möller, J. D., and R. K. Smith, 1994: The development of potential vorticity in a hurricane-like vortex. *Quart. J. Roy. Meteor. Soc.*, **120**, 1255–1265, doi: [10.1002/qj.49712051907](https://doi.org/10.1002/qj.49712051907).
- Montgomery, M. T., and L. J. Shapiro, 1995: Generalized Charney-Stern and Fjørtoft theorems for rapidly rotating vortices. *J. Atmos. Sci.*, **52**, 1829–1833, doi: [10.1175/1520-0469\(1995\)052<1829:GCAFTF>2.0.CO;2](https://doi.org/10.1175/1520-0469(1995)052<1829:GCAFTF>2.0.CO;2).
- Montgomery, M. T., V. A. Vladimirov, and P. V. Denissenko, 2002: An experimental study on hurricane mesovortices. *J. Fluid Mech.*, **471**, 1–32. doi: [10.1017/S0022112002001647](https://doi.org/10.1017/S0022112002001647).
- Nolan, D. S., and L. D. Grasso, 2003: Nonhydrostatic, three-dimensional perturbations to balanced, hurricane-like vortices. Part II: Symmetric response and nonlinear simulations. *J. Atmos. Sci.*, **60**, 2717–2745, doi: [10.1175/1520-0469\(2003\)060<2717:NTPTBH>2.0.CO;2](https://doi.org/10.1175/1520-0469(2003)060<2717:NTPTBH>2.0.CO;2).
- Nolan, D. S., and M. T. Montgomery, 2002: Nonhydrostatic, three-dimensional perturbations to balanced, hurricane-like vortices. Part I: Linearized formulation, stability, and evolution. *J. Atmos. Sci.*, **59**, 2989–3020, doi: [10.1175/1520-0469\(2002\)059<2989:NTDPTB>2.0.CO;2](https://doi.org/10.1175/1520-0469(2002)059<2989:NTDPTB>2.0.CO;2).
- Rozoff, C. M., J. P. Kossin, W. H. Schubert, and P. J. Mulero, 2009: Internal control of hurricane intensity: The dual nature of potential vorticity mixing. *J. Atmos. Sci.*, **66**, 133–147, doi: [10.1175/2008JAS2717.1](https://doi.org/10.1175/2008JAS2717.1).
- Schechter, D. A., and M. T. Montgomery, 2004: Damping and pumping of a vortex Rossby wave in a monotonic cyclone: Critical layer stirring versus inertia-buoyancy wave emission. *Phys. Fluids*, **16**, 1334–1348, doi: [10.1063/1.1651485](https://doi.org/10.1063/1.1651485).
- Schubert, W. H., and B. T. Alworth, 1987: Evolution of potential vorticity in tropical cyclones. *Quart. J. Roy. Meteor. Soc.*, **113**, 147–162, doi: [10.1002/qj.49711347509](https://doi.org/10.1002/qj.49711347509).
- Schubert, W. H., M. T. Montgomery, R. K. Taft, T. A. Guinn, S. R. Fulton, J. P. Kossin, and J. P. Edwards, 1999: Polygonal eyewalls, asymmetric eye contraction, and potential vorticity mixing in hurricanes. *J. Atmos. Sci.*, **56**, 1197–1223, doi: [10.1175/1520-0469\(1999\)056<1197:PEAECA>2.0.CO;2](https://doi.org/10.1175/1520-0469(1999)056<1197:PEAECA>2.0.CO;2).
- Shapiro, L. J., and J. L. Franklin, 1995: Potential vorticity in Hurricane Gloria. *Mon. Wea. Rev.*, **123**, 1465–1475. doi: [10.1175/1520-0493\(1995\)123<1465:PVIHG>2.0.CO;2](https://doi.org/10.1175/1520-0493(1995)123<1465:PVIHG>2.0.CO;2).
- Stern, D. P., and D. S. Nolan, 2009: Reexamining the vertical structure of tangential winds in tropical cyclones: Observations and theory. *J. Atmos. Sci.*, **66**, 3579–3600, doi: [10.1175/2009JAS2916.1](https://doi.org/10.1175/2009JAS2916.1).
- Terwey, W. D., and M. T. Montgomery, 2002: Wavenumber-2 and wavenumber- $m$  vortex Rossby wave instabilities in a generalized three-region model. *J. Atmos. Sci.*, **59**, 2421–2427, doi: [10.1175/1520-0469\(2002\)059<2421:WAWMVR>2.0.CO;2](https://doi.org/10.1175/1520-0469(2002)059<2421:WAWMVR>2.0.CO;2).
- Tung, K. K., 1986: Nongeostrophic theory of zonally averaged circulation. Part I: Formulation. *J. Atmos. Sci.*, **43**, 2600–2618, doi: [10.1175/1520-0469\(1986\)043<2600:NTOZAC>2.0.CO;2](https://doi.org/10.1175/1520-0469(1986)043<2600:NTOZAC>2.0.CO;2).
- Willoughby, H. E., 1998: Tropical cyclone eye thermodynamics. *Mon. Wea. Rev.*, **126**, 3053–3067, doi: [10.1175/1520-0493\(1998\)126<3053:TCET>2.0.CO;2](https://doi.org/10.1175/1520-0493(1998)126<3053:TCET>2.0.CO;2).
- Wu, C.-C., H.-J. Cheng, Y. Wang, and K.-H. Chou, 2009: A numerical investigation of the eyewall evolution in a landfalling typhoon. *Mon. Wea. Rev.*, **137**, 21–40, doi: [10.1175/2008MWR2516.1](https://doi.org/10.1175/2008MWR2516.1).
- Yau, M. K., Y. Liu, D.-L. Zhang, and Y. Chen, 2004: A multiscale numerical study of Hurricane Andrew (1992). Part VI: Small-scale inner-core structures and wind streaks. *Mon. Wea. Rev.*, **132**, 1410–1433, doi: [10.1175/1520-0493\(2004\)132<1410:AMNSOH>2.0.CO;2](https://doi.org/10.1175/1520-0493(2004)132<1410:AMNSOH>2.0.CO;2).